

Estimating crustal seismic anisotropy with a joint analysis of radial and transverse receiver function data

Huafeng Liu and Fenglin Niu

Department of Earth Science, Rice University, 6100 Main Street, Houston, TX 77005, USA. E-mail: hl9@rice.edu

Accepted 2011 September 23. Received 2011 September 23; in original form 2011 May 23

SUMMARY

We developed an integrated technique for estimating crustal anisotropy with a horizontal axis using radial (R) and transverse (T) receiver functions. The technique includes computing three individual and one joint objective function (JOF) and a reliability analysis of the estimated anisotropy. The individual objective functions (IOFs) are designed to: (1) maximize the peak energy of the stacked R receiver function after a cosine moveout correction in the P_s arrival time; (2) to maximize the correlation of the radial receiver functions after a full correction of anisotropy or (3) to minimize the total energy of transverse receiver functions stacked after a removal of crustal anisotropy. The JOF was computed by a weighted average of the three IOFs, and the reliability analysis uses the principle that stacking coherent signals can lead to an increase of signal-to-noise ratio. We applied the technique to synthetic receiver functions generated with 30–60 per cent white noise from a variety of anisotropic and heterogeneous models. The synthetic tests indicate that the proposed technique has good capability to recover the input models. Despite the presence of random and other coherent noises, such as those caused by inhomogeneous structures, in the data, the technique can always provide accurate estimates of crustal anisotropy. We applied the technique to two permanent seismic stations in western China and found significant crustal anisotropy beneath one station located at the northern edge of the Tibetan plateau. The observed fast polarization direction at this station follows the direction of the maximum horizontal tensile stress, suggesting that the observed seismic anisotropy is likely caused by mineral alignment in the lower crust. The station situated in the Sichuan basin, on the other hand, shows little to no seismic anisotropy, which may suggest that the crust beneath the basin is nearly rigid with very little deformation. The developed technique can be applied to any broadband seismic stations that have a good backazimuthal coverage of teleseismic events.

Key words: Body waves; Seismic anisotropy; Statistical seismology; Crustal structure.

1 INTRODUCTION

Numerous seismic observations have shown that the Earth's upper crust and upper mantle exhibit anisotropy for seismic wave propagation (e.g. Crampin & Lovell 1991; Silver 1996). It is generally believed that seismic anisotropy observed in the upper crust is caused by stress-induced alignment of cracks. As the vertical stress increase steadily with depth, the minimum stress direction starts to lie in a horizontal direction below a critical depth of 0.5–1 km (Crampin & Chastin 2003). Such a stress field leads to the development of vertical cracks and azimuthal anisotropy. On the other hand, seismic anisotropy observed in the upper mantle is generally believed to be caused by preferentially orientation of the highly anisotropic upper-mantle mineral, olivine, through mantle deformation (e.g. Nicolas & Christensen 1987). The close relationship between the stress-strain field and seismic anisotropy thus can be

used to map deformation associated with a wide range of tectonic processes.

Seismic anisotropy is often measured with two parameters, the fast polarization direction φ and delay time δt between the fast and slow directions, from splitting or birefringence of shear waves, such as the S , ScS and SKS phases, recorded at either local or teleseismic distances (e.g. Crampin 1987; Silver & Chan 1991). Kaneshima (1990) measured φ and δt using direct S waves recorded at ~ 40 seismic stations across Japan from local earthquakes with a focal depth ranging from 1.5 to 100 km. The fast polarization direction φ measured at most of the stations aligns well with the direction of the maximum horizontal compressional stress. The observed δt varies between 0.03 and 0.2 s and appears to increase with focal depth for earthquakes occurring shallower than 15 km. The correlation was not seen from events with a deeper focus, including those occurring in the mantle. The result suggests that the source region producing

the observed splits is most likely located in the upper 15 km of the crust and seismic anisotropy in the lower crust is relatively weak. However, if seismic anisotropy changes with depth and if local earthquakes are restricted to certain backazimuths, the local S-wave data could have very limited resolution of anisotropy in the lower crust, as the measured φ and δt could, in principle, reflect only the seismic anisotropy of the last travelled path, which is the upper crust.

Seismic anisotropy in the mantle is usually measured with the teleseismic SKS wave, a radially polarized phase at the core–mantle boundary (CMB) right after the P -to- S conversion. The observed seismic anisotropy could, in principle, be located anywhere along the S-wave ray path from the CMB to the surface at the receiver side. Although the dominant contribution to the splitting can be attributed to the upper mantle above the transition zone, as splitting parameters measured from different types of shear waves recorded at a seismic station appear to be consistent with each other (Silver & Chan 1991; Meade *et al.* 1995; Niu & Perez 2004), it is always difficult to pinpoint the exact depth range within the upper mantle for the observed anisotropy (Silver 1996). Comparison with patterns of lithospheric deformation and asthenospheric flow are usually used to argue for the possible source region of the observed seismic anisotropy. For example, Masy *et al.* (2011) attributed the large splitting times observed at the Caribbean–South American Plate boundary to a mantle flow induced by slab tears and the moderate splitting times from the Merida Andes to vertical coherent deformation in the lithosphere. Another ambiguity in interpreting SKS splitting is the crustal contribution. Although many studies indicate that splitting times because of upper crustal anisotropy is less than 0.2 s, as mentioned above, contributions from the lower crust is still unclear. This is particularly true in regions where lower crustal flow may be present, like in the eastern margin of Tibetan plateau (Clark & Royden 2000).

McNamara & Owens (1993) found clear evidence of waveform splitting of the Moho Ps converted phase recorded at seismic stations in the Basin and Range province in the United States. They applied several shear wave splitting analysis techniques developed for SKS/SKKS measurements (e.g. Bowman & Ando 1987; Silver & Chan 1991) to the Moho Ps conversion data and obtained a delay time of ~ 0.2 s. They found that the fast polarization directions at all the stations are either parallel or subparallel to the direction of maximum horizontal tensile stress. This is inconsistent with the upper crustal anisotropy mechanism discussed above; rather it suggests that preferred alignment of anisotropic minerals, which is used in interpreting mantle anisotropy, is the likely mechanism here. Nagaya *et al.* (2008) also applied the splitting measurement techniques to receiver function data recorded in the Chugoku region of southwestern Japan. The fast polarization directions obtained from the Moho Ps conversion phase appeared to be also in the direction of maximum horizontal tensile stress and normal to those from local earthquake measurements obtained by Kaneshima (1990). The observed splitting time ranges from 0.2 to 0.7 s, which should be no longer negligible in interpreting SKS splitting data. A robust estimate of crustal seismic anisotropy thus is not only critical in understanding crustal deformation, but also of great importance in deciphering dynamic processes at various depths in the upper mantle.

In general, the Moho Ps converted wave is a much weaker signal compared to the SKS/SKKS phase. As shown later, the techniques designed for extracting splitting parameters from individual SKS/SKKS waveform data could introduce significant measurement errors and may not be appropriate to receiver function data. To ob-

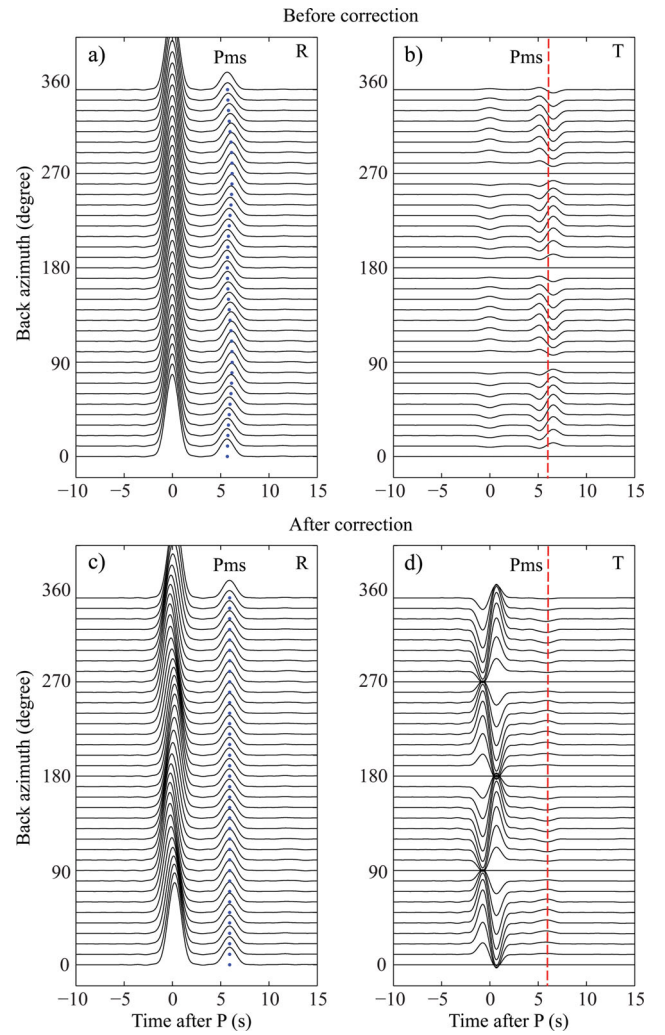


Figure 1. Synthetic receiver functions computed from a one-layered anisotropy model (M1 in Table 1) are plotted as a function of backazimuth. The T receiver functions shown in (b) and (d) are magnified by a factor of 2. The R and T components before correction of anisotropy are shown in (a) and (b), respectively. Dots in (a) indicate the arrival time of the peak amplitude of the Moho Ps converted phase. Note its cosine variation along the backazimuthal direction. Dashed line in (b) indicates the Ps arrival time. Note that the polarity of the Ps phase changes periodically with a period of 180° . The R and T receiver functions after the removals of anisotropy are shown in (c) and (d), respectively. Again, dots in (c) indicate the peak of the Moho Ps wave. Note the excellent alignment of the Ps after the correction. The dashed line in (d) also indicates the Ps arrival time, around where little to no energy remained after the removal of seismic anisotropy.

tain robust estimates of seismic anisotropy from receiver function data, synthetic receiver function data from anisotropy velocity models have been computed for comparison (Levin & Park 1997; Peng & Humphreys 1997; Savage 1998; Frederiksen & Bostock 2000). Synthetic receiver functions show a clear $\cos 2\theta$ variation in the peak Ps arrival time on the radial (R) receiver functions (Fig. 1a) and in the polarity of the Ps waveform on the transverse (T) receiver functions (Fig. 1b) in the presence of crustal anisotropy with a horizontal axis. These features have been used to identify crustal anisotropy and extract splitting parameters from receiver function data. Levin *et al.* (2008) employed a forward modelling approach to match directional gathers of receiver functions with synthetics computed from anisotropic models. To better constrain the

models, they first used the polarity change observed in the transverse component to define the fast direction.

In this study, we developed a splitting measurement technique specifically for receiver function data. It uses the features that are uniquely possessed by anisotropic models observed on the synthetic receiver function data (Fig. 1). As mentioned before, the Moho P_s conversion usually has low signal-to-noise ratio (SNR) in individual receiver function data. We thus decided to solve one pair of φ and δt that best explain all the receiver functions recorded at a single station, instead of using the approach employed by the previous studies (McNamara & Owens 1993; McNamara *et al.* 1994; Nagaya *et al.* 2008), which measures individual (φ , δt) sequentially from receiver functions and selects the most frequent occurring pair as the station estimate. We further verify our estimates with a statistical analysis based on SNR improvement of the P_s arrival as a SNR on the radial/transverse component after the estimated seismic anisotropy being corrected. We conducted extensive tests with synthetic receiver functions and found that the technique was able to recover the input anisotropy in the presence of high level of noise in the data and certain complexities in crustal structure, such as a dipping CMB and azimuthal variations in velocity structure. We further applied this technique to two permanent stations in western China and found that our measurements are consis-

tent with previous studies, suggesting that the method could be used to systematically map crustal anisotropy at regional or global scale.

2 METHOD

2.1 Receiver function generation and moveout corrections

We used the ‘water level’ deconvolution technique to generate R and T receiver functions (Clayton & Wiggins 1976; Ammon 1991), a modified division in the frequency domain:

$$\begin{aligned} F_r(\omega) &= R(\omega)Z^*(\omega)e^{-\left(\frac{\omega}{2a}\right)^2}/\max\{Z(\omega)Z^*(\omega), k|Z_{\max}(\omega_0)|^2\} \\ F_t(\omega) &= T(\omega)Z^*(\omega)e^{-\left(\frac{\omega}{2a}\right)^2}/\max\{Z(\omega)Z^*(\omega), k|Z_{\max}(\omega_0)|^2\}. \end{aligned} \quad (1)$$

Here k and a are two constants that define the ‘water level’ and the corner frequency of the Gaussian low-pass filter, respectively. k was set to be 0.01 and a was set to be 4.0, which is equivalent to a corner frequency of ~ 1 Hz. $Z(\omega)$ and $R(\omega)$ are the spectra of the radial and transverse components of the seismic recordings and $Z^*(\omega)$ is the complex conjugate of $Z(\omega)$. Once they were generated,

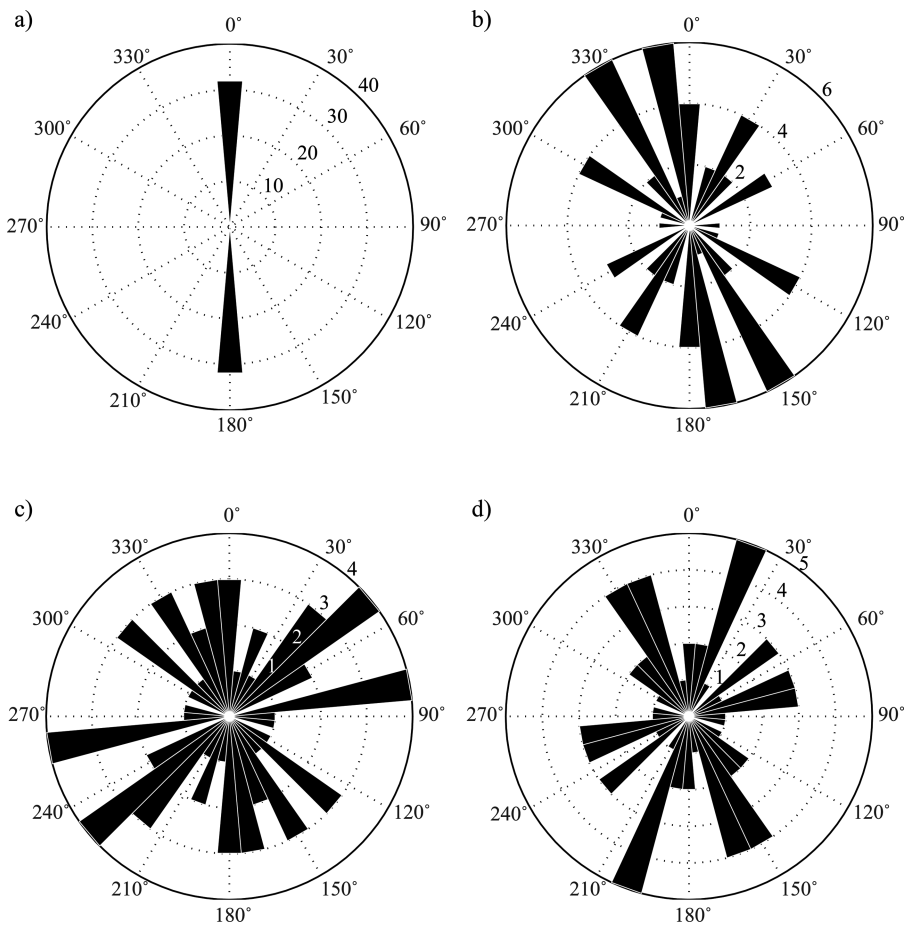


Figure 2. Rose diagrams showing fast polarization directions estimated from individual synthetic receiver functions computed with the anisotropic model M1 and noise levels of (a) 0 per cent, (b) 30 per cent and (c) 60 per cent. We used a 10° bin in plotting the measurements. Numbers near the circular grid indicate the total numbers of measurement within a particular bin. Note the significant difference in the estimates of the fast direction when noise is present in the data (b and c). The estimated fast directions are spread in the full backazimuthal range when the noise level is high (c). We also calculated synthetic receiver functions using a one-layer isotropic model (M2 in Table 1) and included 30 per cent white noise. The estimated apparent fast direction is shown in (d), which also exhibits substantial variations.

we normalized the R and T receiver functions by a division of the total energy computed from the two components in the time window between -10 and 40 s.

Because the Moho P_s conversion phase has a slightly smaller ray parameter than the direct P wave does, the relative arrival time of the P_s phase with respect to the P wave has a negative moveout. We used a revised IASP91 velocity model (Kennett & Engdahl 1991) with a modified crust to compute this moveout and made corrections so that all the P_s phases have a relative arrival time equivalent to the epicentral distance of 60° with a source depth of 0 km. After normalization and moveout correction, the R and

T receiver functions were plotted as a function of backazimuth to show whether there are systematic variations in the peak P_s arrival time and polarity changes in the R and T receiver functions, respectively.

2.2 Estimating shear-wave splitting with individual receiver function

Most previous crustal anisotropy studies with receiver function data (e.g. McNamara & Owens 1993; McNamara *et al.* 1994; Iidaka &

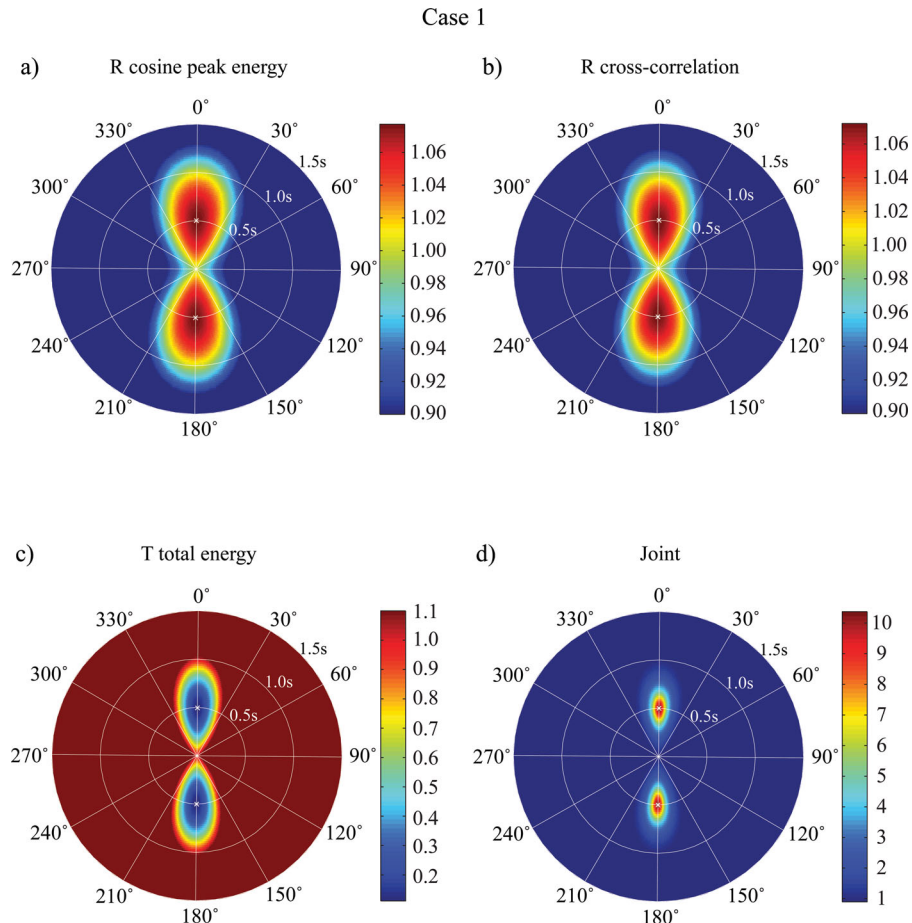


Figure 3. Results from test case 1. The three IOFs defined by the equations 6, 7 and 8 are shown in (a), (b) and (c), respectively. Synthetic receiver functions were calculated using the anisotropic model, M1 (Table 1), with 0 per cent noise. The objective functions were computed in a 2-D plane of $(\varphi, \delta t)$ in the range of $(0^\circ\text{--}360^\circ, 0.0\text{--}1.5$ s) with an increment of $(1^\circ, 0.02$ s). (a), (b) and (c) correspond to three different ways for estimating seismic anisotropy: (1) R energy maximization with cosine moveout correction; (2) Radial cc maximization and (c) T energy minimization. Colour scales showing variations of the objective functions are plotted right to the functions. The JOF is shown in (d). The input fast polarization direction and the splitting time are marked by a white 'x'.

Table 1. Crust models used for synthetic tests.

| Model description | H (km) | α (km s^{-1}) | β (km s^{-1}) | ρ (g cm^{-3}) | Fast direction | S-wave anisotropy | Strike | Dipping |
|-------------------|------------------------------------|------------------------------------|-----------------------------------|----------------------------------|----------------|-------------------------|--------------------------|-----------|
| M1 | 1-layer flat_aniso. | 50.0 | 6.50 | 3.75 | 2.9 | 0° | 4 per cent | – |
| M2 | 1-layer flat_iso. | 50.0 | 6.50 | 3.75 | 2.9 | – | – | – |
| M3 | 1-layer dip_iso. | 50.0 | 6.50 | 3.75 | 2.9 | – | – | 0° |
| M4 | 1-layer het._iso. | 50.0 | 6.50 | 3.60 3.75 | 2.9 | – | – | – |
| M5 | 2-layer flat_aniso. | 20.0 30.0 | 5.80 6.50 | 3.36 3.75 | 2.7 2.9 | 60° 0° | 2 per cent 4 per cent | – |
| M6 | 1-layer flat_iso. aniso. mantle | 50.0 50.0 | 6.50 8.04 | 3.75 4.50 | 2.9 3.3 | – 0° | – 4 per cent | – – |

Table 2. List of cases tested with synthetic data.

| Case | Velocity model | Backazimuth distribution | Noise level | φ | δt (s) | I_{\max} | SNRT analysis |
|------|----------------|--------------------------|-------------|-----------|----------------|------------|-----------------------|
| 1 | M1 | Full | 0 per cent | 0° | 0.50 | 10.372 | Positive ^a |
| 2 | M1 | Full | 30 per cent | 3° | 0.48 | 1.866 | Positive ^a |
| 3 | M1 | Full | 60 per cent | -4° | 0.50 | 1.353 | Positive ^a |
| 4 | M1 | Real | 30 per cent | 3° | 0.48 | 1.781 | Positive ^a |
| 5 | M2 | Full | 30 per cent | -40° | 0.10 | 1.034 | Negative |
| 6 | M3 | Full | 30 per cent | -27° | 0.04 | 1.003 | Negative |
| 7 | M3 | One side | 30 per cent | 9° | 0.18 | 1.084 | Negative |
| 8 | M4 | Full | 30 per cent | 12° | 0.10 | 1.043 | Negative |
| 9 | M5 | Full | 30 per cent | 16° | 0.30 | 1.280 | Positive ^a |
| 10 | M6 | Full | 30 per cent | 70° | 0.06 | 1.002 | Negative |

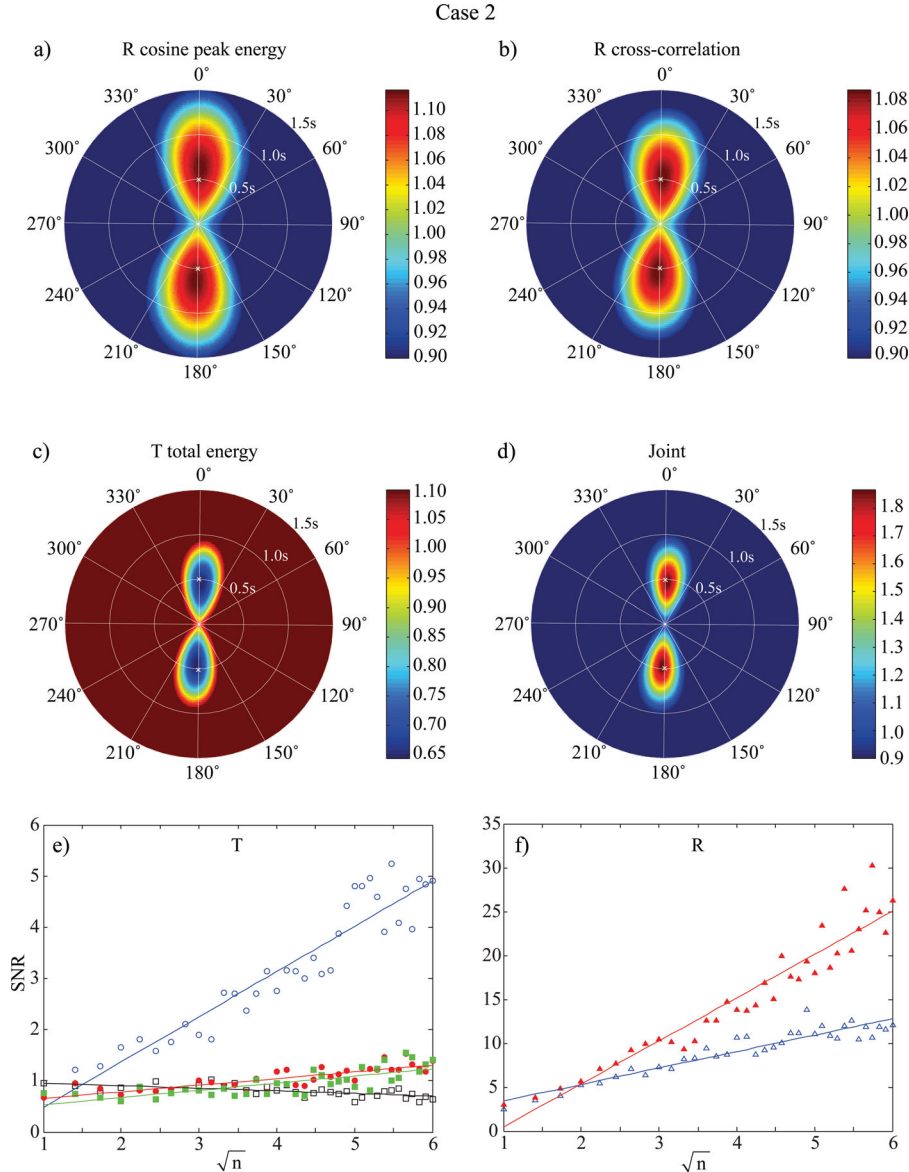
^aAnisotropic crust cases.

Figure 4. Results from test case 2. (a–d) here are similar to (a–d) shown in Fig. 3, except that the synthetic receiver functions were computed using the anisotropic model, M1 (Table 1), with 30 per cent white noise. Results of the SNRT analysis with the T and R receiver function data are shown in (e) and (f), respectively. Open and filled symbols represent SNRs calculated from stacks of receiver functions before and after the removal of seismic anisotropy determined by the JOF. Results from stacks of the T receiver functions with an appropriate change in waveform polarity are shown in circles and those from stacks of T and R receiver function without sign changes are indicated by squares and triangles, respectively. Solid lines indicate results from linear regressions of each group. Note the steady increase of circles (stack with a sign correction) with increasing $N^{1/2}$ in (e) and that the filled triangles are always above the open ones in (f).

Niu, 2001; Nagaya *et al.* 2008) employed more or less the same techniques developed for SKS splitting analysis (e.g. Bowman & Ando 1987; Silver & Chan 1991). The analysis involves a grid search of φ and δt and can be divided roughly into four major steps: (1) projecting each receiver function pair [$F_r(t)$ and $F_t(t)$] to the assumed fast and slow polarization directions $F_f(t, \varphi)$ and $F_s(t, \varphi)$;

$$\begin{aligned} F_f(t, \varphi) &= F_r(t) \cdot \cos(\varphi - \theta) + F_t(t) \cdot \sin(\varphi - \theta), \\ F_s(t, \varphi) &= -F_r(t) \cdot \sin(\varphi - \theta) + F_t(t) \cdot \cos(\varphi - \theta) \end{aligned} \quad (2)$$

where θ is the backazimuth of the individual receiver function; (2) time shifting the fast component [$F_f(t, \varphi)$] forward and the slow component [$F_s(t, \varphi)$] backward by half of the assumed splitting time (δt) to form the corrected fast and slow components [$F_f^c(t, \varphi, \delta t)$ and $F_s^c(t, \varphi, \delta t)$]

$$\begin{aligned} F_f^c(t, \varphi, \delta t) &= F_f(t + \delta t/2, \varphi) \\ F_s^c(t, \varphi, \delta t) &= F_s(t - \delta t/2, \varphi); \end{aligned} \quad (3)$$

(3) projecting the time-corrected receiver-function pair [$F_f^c(\varphi, \delta t, t)$ and $F_s^c(\varphi, \delta t, t)$] back to the R and T directions [$F_r^c(\varphi, \delta t, t)$ and $F_t^c(\varphi, \delta t, t)$; Figs 1c and d]

$$\begin{aligned} F_r^c(t, \varphi, \delta t) &= F_f^c(t, \varphi, \delta t) \cdot \cos(\varphi - \theta) - F_s^c(t, \varphi, \delta t) \cdot \sin(\varphi - \theta) \\ F_t^c(t, \varphi, \delta t) &= F_f^c(t, \varphi, \delta t) \cdot \sin(\varphi - \theta) + F_s^c(t, \varphi, \delta t) \cdot \cos(\varphi - \theta) \end{aligned} \quad (4)$$

and (4) searching for a pair of $(\varphi, \delta t)$ that either minimizes the T component energy or maximizes the cross correlation [$c(\varphi, \delta t)$] between the time-corrected fast and slow components

$$c(\varphi, \delta t) = \int_{t_b}^{t_e} F_f^c(t, \varphi, \delta t) \cdot F_s^c(t, \varphi, \delta t) dt \quad (5)$$

here $[t_b, t_e]$ defines the arrival time window of the Moho Ps converted phase.

The above procedure is usually applied to each receiver function pair which yields multiple estimates of $(\varphi, \delta t)$ at each seismic station. The most frequently observed φ is usually taken as the measurement

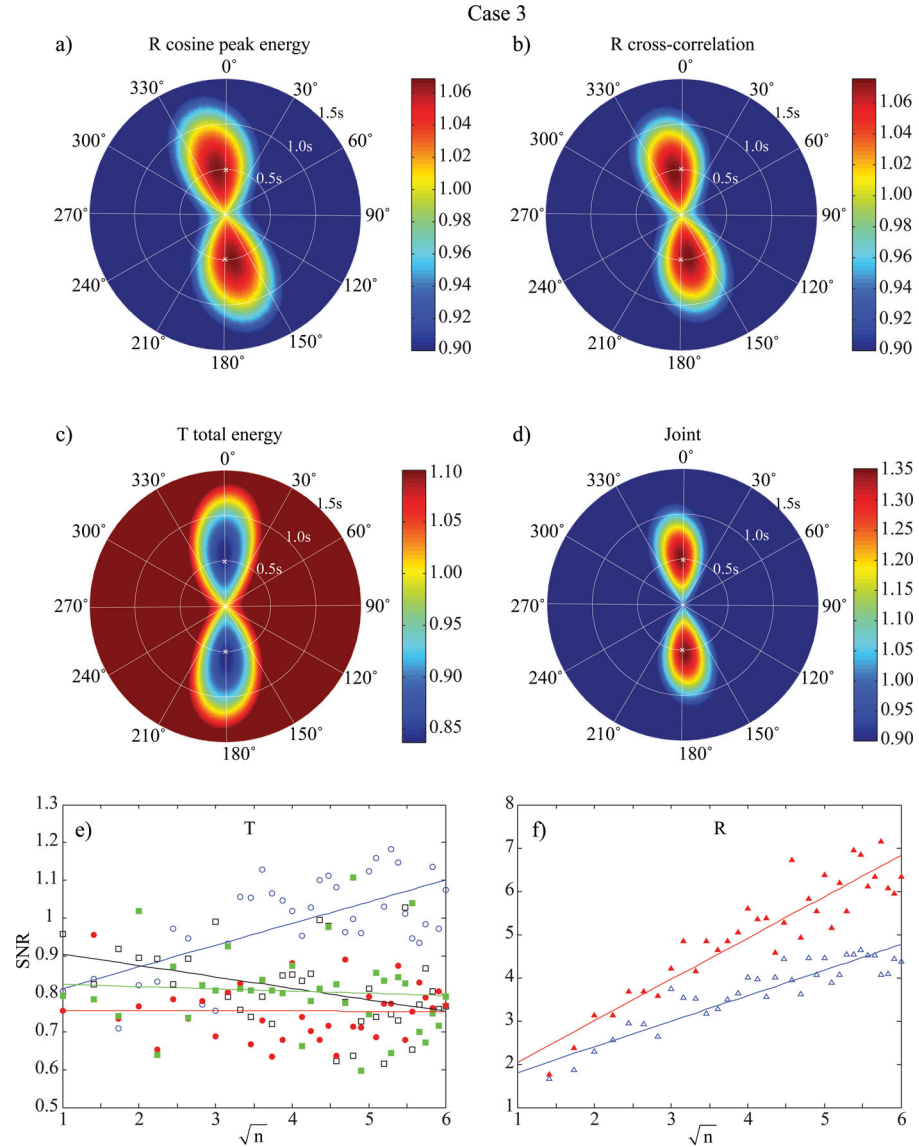


Figure 5. Results from test case 3. Same as Fig. 4 except that the synthetic receiver functions were computed with the same M1 model but a higher noise level (60 per cent). The SNRT analysis shows similar features to those in Fig. 4.

at the station and the delay time is computed from the average of the δt estimates (Nagaya *et al.* 2008). We have applied this single-event based method to several synthetic data sets and found that it provides reliable splitting estimates only when noise level in the data is low (Fig. 2a). Even a small amount of noise (30 per cent) could bias the estimate of fast polarization direction by as much as 30° (Fig. 2b). Moreover, at high noise level, the measured fast directions are highly scattered and appear to be insensitive to the input model (Figs 2c and d).

2.3 Imaging shear wave splitting with a joint analysis of receiver function gathers

As shown above, in the presence of noise, measuring splitting parameters from individual receiver function data could introduce large errors. We chose to solve for one pair of $(\varphi, \delta t)$ that fits all the receiver functions collected at a station. We further combined

the results from three different methods to seek a robust estimate of crustal anisotropy with receiver function data.

2.3.1 Radial energy maximization with cosine moveout correction

Fig. 1(a) shows a four-lobed variation in the peak P_s arrival time, which can be evaluated by a cosine function. The fast direction and delay time can be estimated from the phase and amplitude of the cosine function. Our first means of estimating $(\varphi, \delta t)$ is thus based on the ratio of peak energy computed by stacking all the R receiver functions after and before the time correction of the cosine moveout

$$I_{r \cos}(\varphi, \delta t) = \frac{\left\{ \sum_{j=1}^N F_r^j \left[t - \frac{\delta t}{2} \cos 2(\varphi - \theta_j) \right] \right\}_{\max}^2}{\left\{ \sum_{j=1}^N F_r^j(t) \right\}_{\max}^2}, \quad t \in [t_b, t_e]. \quad (6)$$

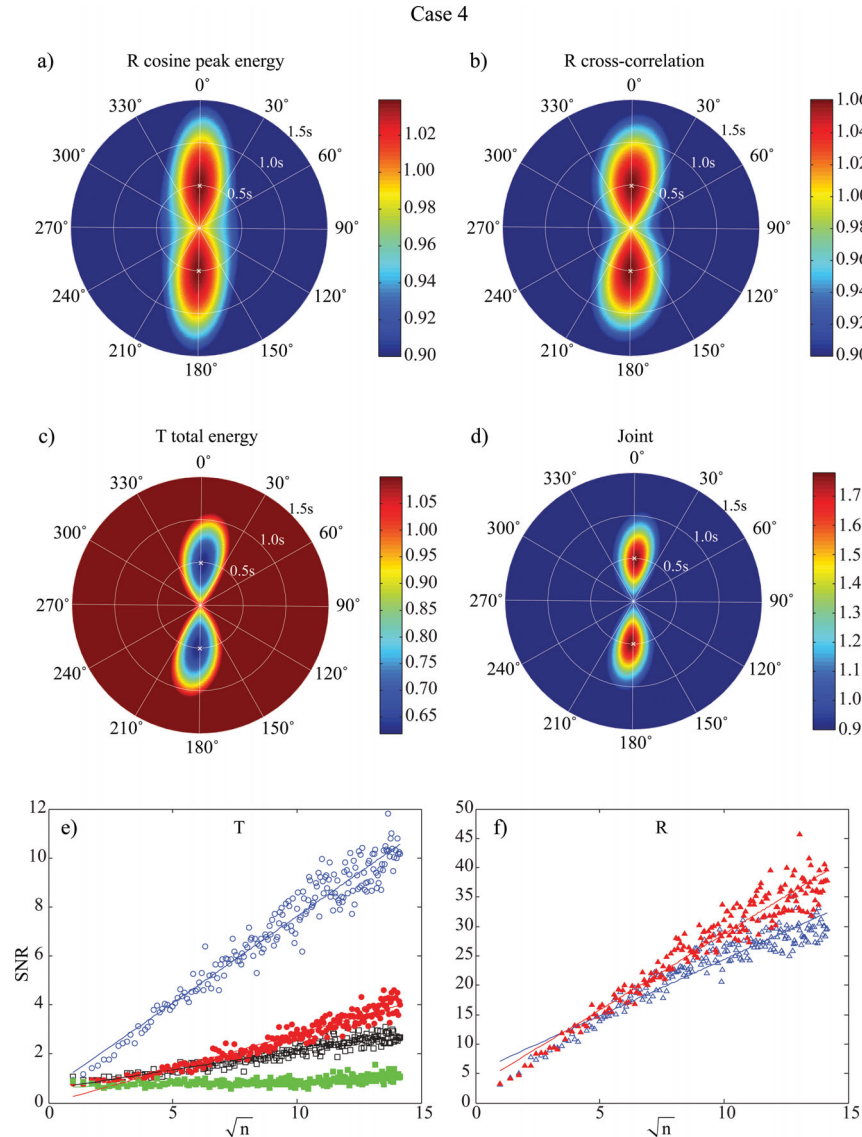


Figure 6. Results from test case 4. Same as Fig. 4 except that the synthetic receiver functions have a different coverage in backazimuth. The backazimuthal distribution of 200 events recorded at station XJYCH was used here. Both the SNRT analysis and the high maximum value of the JOF indicate the existence of seismic anisotropy in the data.

The superscript j here represents the j th receiver function with a backazimuth θ_j . N is the total number of receiver functions. The subscript max indicates the largest amplitude within the P_s arrival time window defined by $[t_b, t_e]$. An example of the peak energy ratio as a function of $(\varphi, \delta t)$ is shown in Fig. 3(a). We varied φ in the range of $0\text{--}360^\circ$ with an increment of 1° and δt from 0.0 to 1.5 s in increments of 0.02 s. The ratio reaches its maximum at the input anisotropic parameters ($\varphi = 0^\circ$, $\delta t = 0.5$ s; Fig. 3a).

2.3.2 Radial correlation coefficient (cc) maximization

We further used the cross correlation of the R receiver functions to estimate the splitting parameters φ and δt . This is done first by following the eqs (2)–(4) to compute the anisotropy-removed R and T receiver functions. The summed cross correlation coefficient (cc),

normalized by its original value,

$$I_{rc}(c, \delta t) = \frac{\int_{t_b}^{t_e} \left\{ \left[\sum_{j=1}^N F_{r,j}^c(\varphi, \delta t, t) \right]^2 - \sum_{j=1}^N [F_{r,j}^c(\varphi, \delta t, t)]^2 \right\} dt}{\int_{t_b}^{t_e} \left\{ \left[\sum_{j=1}^N F_{r,j}(t) \right]^2 - \sum_{j=1}^N [F_{r,j}(t)]^2 \right\} dt} \quad (7)$$

is used in evaluating the best fit for the crustal anisotropy. With synthetic receiver function data, this approach also recovered the input splitting parameters ($\varphi = 0^\circ$, $\delta t = 0.5$ s; Fig. 3b).

2.3.3 Transverse energy minimization

This is an implementation of Silver & Chan (1991) applied to data from multiple events (Wolfe & Silver 1998; Li & Niu 2010; Masy

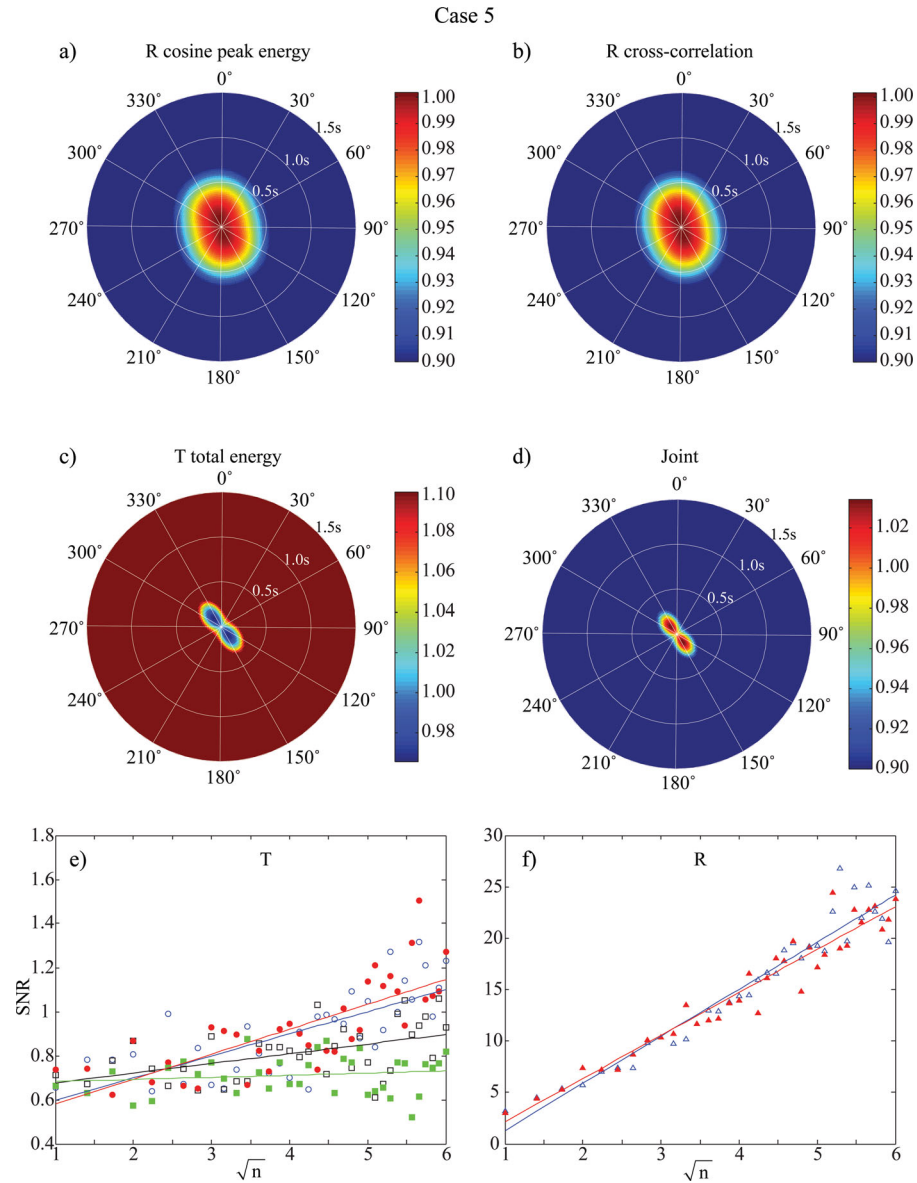


Figure 7. Results from test case 5. Same as Fig. 4 except that the synthetic receiver functions were computed using the one-layered isotropic model, M2 with 30 per cent white noise. The SNRT analysis doesn't show any characteristic features of seismic anisotropy, which is also consistent with the low maximum value of the JOF.

et al. 2011). Normally, the Moho P_s converted phase is radially polarized; therefore, the presence of T energy is indicative for inhomogeneous structure in the crust. For an assumed pair of $(\varphi, \delta t)$, we first followed the eqs (2)–(4) to compute the T energy after the time correction and then used its ratio with the original T energy to estimate the crustal anisotropy

$$I_t(\varphi, \delta t) = \frac{\sum_{j=1}^N \int_{t_b}^{t_e} [F_{t,j}^c(\varphi, \delta t, t)]^2 dt}{\sum_{j=1}^N \int_{t_b}^{t_e} [F_{t,j}(t)]^2 dt}. \quad (8)$$

Here the subscript j and superscript c indicate the j th receiver function after time correction. N is the total number of receiver functions and the P_s arrival time window is defined by $[t_b, t_e]$. As shown in Fig. 3(c), the method recovers the anisotropy ($\varphi = 0^\circ$, $\delta t = 0.5$ s) used for computing synthetic receiver functions.

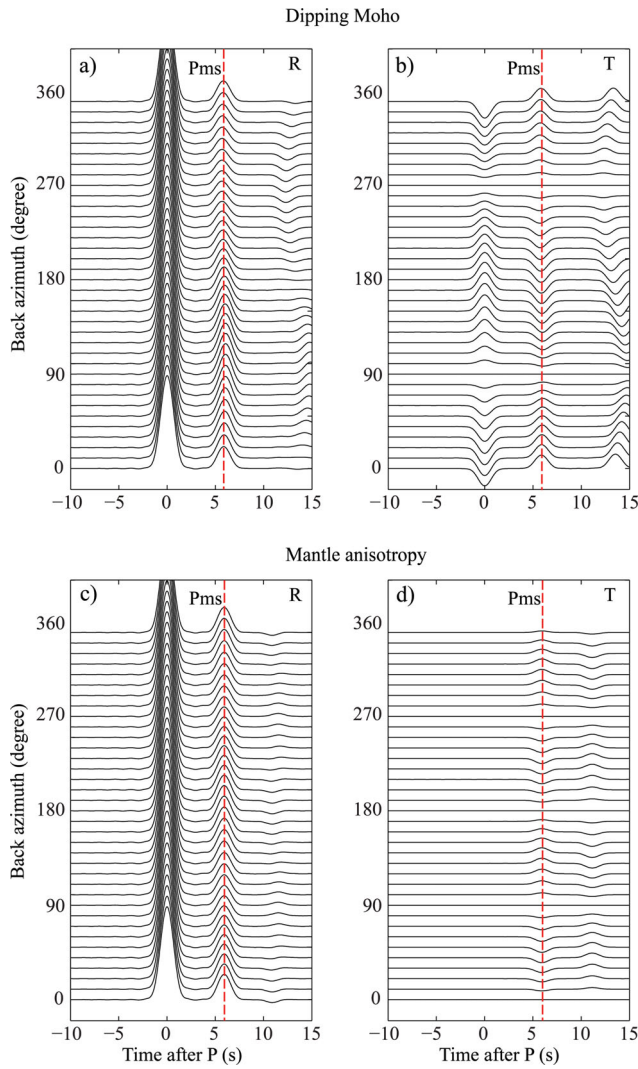


Figure 8. Synthetic R and T receiver functions computed from the dipping Moho model, M3 in Table 1 and the anisotropic mantle model, M6 in Table 1 are shown in (a, b) and (c, d), respectively. All are plotted as a function of backazimuth. The T receiver functions shown in (b) and (d) are magnified by a factor of 2.

2.3.4 Joint solution

The above three methods use different characteristics of crustal anisotropy on receiver function data. In principle, they are expected to yield more or less the same estimate (Figs 3a–c). However, they could give slightly different or even inconsistent estimates when noise and other inhomogeneous structure are present. To make the full usage of the fingerprint of anisotropy on receiver functions, we combined the three objective functions into a joint objective function (JOF)

$$I(\varphi, \delta t) = \frac{[I_{r\cos}(\varphi, \delta t)]^{w_1} [I_{rc\cos}(\varphi, \delta t)]^{w_2}}{[I_t(\varphi, \delta t)]^{w_3}}, \quad (9a)$$

which can be rewritten as

$$\ln I(\varphi, \delta t) = w_1 \ln I_{r\cos}(\varphi, \delta t) + w_2 \ln I_{rc\cos}(\varphi, \delta t) - w_3 \ln I_t(\varphi, \delta t). \quad (9b)$$

Here w_1 , w_2 and w_3 are the relative weights among the three measurements, which can be determined on the basis of the relative confidence level of the three measurements. We have set them to one in this study for simplicity. An example of the JOF is shown in Fig. 3(d), which exhibits a maximum at the input fast direction and delay time ($\varphi = 0^\circ$, $\delta t = 0.5$ s), as each individual measurement does. Based on eq. (3), the corrected fast and slow components do not change when $\delta t = 0$ s. Consequently, there are no changes in the corrected R and T receiver functions and the ratios defined in the eqs (6)–(8) have a unit value. The JOF thus has a unit value at $\delta t = 0$ s and is expected to have a maximum amplitude greater than one once anisotropy induced waveform splitting is corrected. It can be shown that the significance of maximums (the difference between maximums and unit value) of the three individual objective functions (IOFs) and the subsequent JOF are approximately proportional to δt^2 (see the Appendix). The maximum amplitude of the JOF, thus, is an important indicator of crustal anisotropy imprinted on receiver function data.

2.3.5 SNR test (SNRT)

We further designed a statistical analysis to evaluate whether the estimated anisotropy is a robust feature of data or not. The analysis is based on an algorithm for SNR diagnosis. The anisotropy-corrected R receiver functions are expected to record a coherent P_s converted signal, although the T receiver functions should consist mainly of random noise after the removal of anisotropy. For a coherent signal, a classical way to enhance SNR is stacking, which can improve the SNR by a factor of $N^{1/2}$ when the noise among traces is uncorrelated. We used this criterion to diagnose whether the data in certain time window consists mainly of coherent signals or random noise. We first randomly selected a subsample of N receiver functions from a total of M receiver functions gathered at a seismic station. These receiver functions were stacked linearly and the SNR was calculated from the stacked receiver function. We repeated this procedure for a total of m times (here $m = 100$) and took the geometric mean of the m measurements of SNR

$$\sigma_N = \prod_{k=1}^m \left\{ \int_{signal} \left[\sum_{j=1}^N F_j^k(t, \varphi, \delta t) \right]^2 dt \right. \\ \left. / \int_{noise} \left[\sum_{j=1}^N F_j^k(t, \varphi, \delta t) \right]^2 dt \right\}^{1/m}. \quad (10)$$

Here σ_N represents SNR measured after stacking N receiver functions. $F_j^k(t, \varphi, \delta t)$ indicates the j th receiver function [either R or T,

before ($\delta t = 0$ s) or after delay time correction] in the k th subsample. The signal and noise time windows are taken as the P_s arrival time and a time interval before P . We varied N from 1 to M . For a signal, σ_N is expected to linearly increase with $N^{1/2}$, although for noise σ_N should stay at the same level regardless of an increase of N .

For comparison, we analysed the relationship of σ_N versus $N^{1/2}$ for six types of data: (1) original T receiver function, $F_t(t)$; (2) polarity-corrected T receiver function with no correction of anisotropy, $F_t^p(t)$; (3) anisotropy-corrected T receiver function with no polarity changes, $F_t^c(t, \varphi, \delta t)$; (4) anisotropy-corrected T receiver function with polarity changes, $F_t^{cp}(t, \varphi, \delta t)$; (5) original R receiver function, $F_r(t)$ and (6) anisotropy-corrected R receiver function, $F_r^c(t, \varphi, \delta t)$. In an anisotropic media, the P_s signals on T component have a four-lobed change in waveform polarity. Thus, we would not expect any increase of σ_{N1} for a plain stack of the orig-

inal T receiver functions without considering the polarity changes across backazimuth. On the other hand, σ_{N2} is expected to increase steadily once the polarity changes are taken into account. In other words, we expect σ_{N1} to stay flat and σ_{N2} to increase linearly with $N^{1/2}$. Once crustal anisotropy is corrected, the T receiver functions consist mainly of random noise, so the stacked amplitude will remain roughly similar regardless whether the waveform polarity was switched properly before the stacking. Thus σ_{N3} and σ_{N4} should be independent of N . Meanwhile, the stacked amplitude of anisotropy-corrected R receiver functions is expected to have higher SNR than the stack of the original ones, that is $\sigma_{N6} > \sigma_{N5}$.

3 SYNTHETIC TESTS

We have conducted extensive synthetic tests to examine the reliability and robustness of the joint estimate. In particular, we want

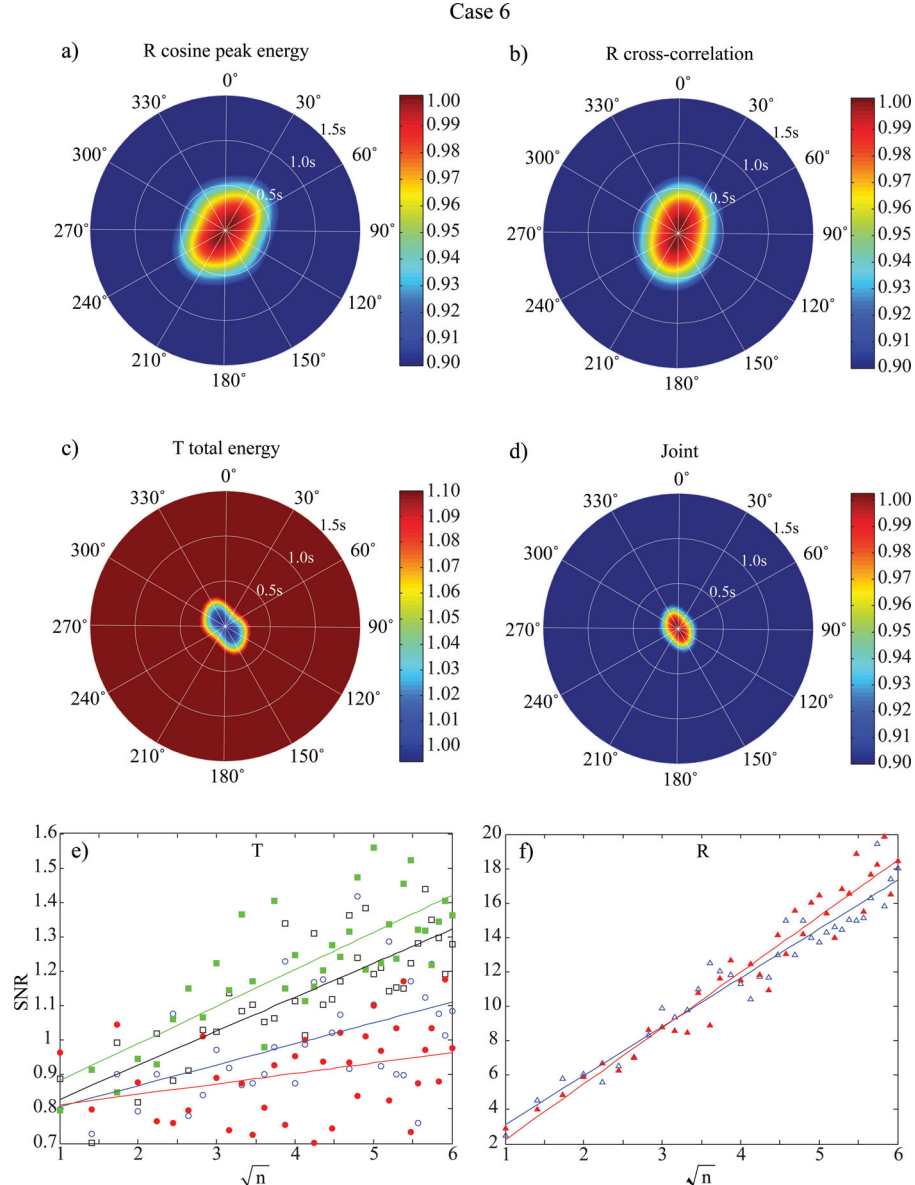


Figure 9. Results from test case 6. Same as Fig. 4 except that the synthetic receiver functions were calculated using the model M3 in Table 1 (a one-layered isotropic crust plus a dipping Moho). Random noise was set to the same 30 per cent level. Note the low maximum value of the JOF shown in (d). The SNRT analysis also indicates no anisotropy in the data. Both results suggest that our integrated analysis can resolve seismic anisotropy from dipping interface when the backazimuthal coverage of the data is good.

to learn: (1) how well the method recovers the input anisotropy including two-layered anisotropic model; (2) how robust the measurement is under the presence of noise, lack of a full coverage in backazimuth and other inhomogeneous structures such as a dipping Moho, azimuthal variation in velocity structure and mantle anisotropy and (3) how significant anisotropy is required from data.

We computed synthetic seismograms with an epicentral distance of 60° and source depth of 0 km using the ray summation method developed by Frederiksen & Bostock (2000). The velocity models used in the synthetic tests are listed in Table 1, which includes: (1) a one-layered anisotropic crust model; (2) a one-layered isotropic crust model; (3) a one-layered isotropic crust with a dipping Moho model; (4) a one-layered heterogeneous crust model with a four-quadrant azimuthal variation in velocity; (5) a two-layered anisotropic crust model and (6) a one-layered isotropic crust model with anisotropic mantle.

Receiver functions were computed using eq. (1) with one of the following backazimuthal coverages: (1) a full coverage in backazimuth (from 0° to 350° in every 10° interval); (2) one side coverage in backazimuth (from 0° to 175° in every 5° interval) or (3) the backazimuth distribution recorded at station XJ.YCH, in Xinjiang province, China (239 receiver functions, with a good coverage in the backazimuthal ranges of 0° – 200° and 270° – 360°). To test the robustness of the joint estimator, we added two levels (30 and 60 per cent) of white noise to the synthetic data. We tested a total of 10 cases, which are listed in Table 2. In the following paragraphs, we show the results from the individual and joint estimators and discuss how well they were able to recover the input models. In all the cases, the joint estimator provided more accurate estimates of the input seismic anisotropy than the individual measurement does. In test case 1, synthetic receiver functions were computed with a one-layered anisotropic crust model (M1 in Table 1) without adding any noise and, thus, each of the individual measurements was able to

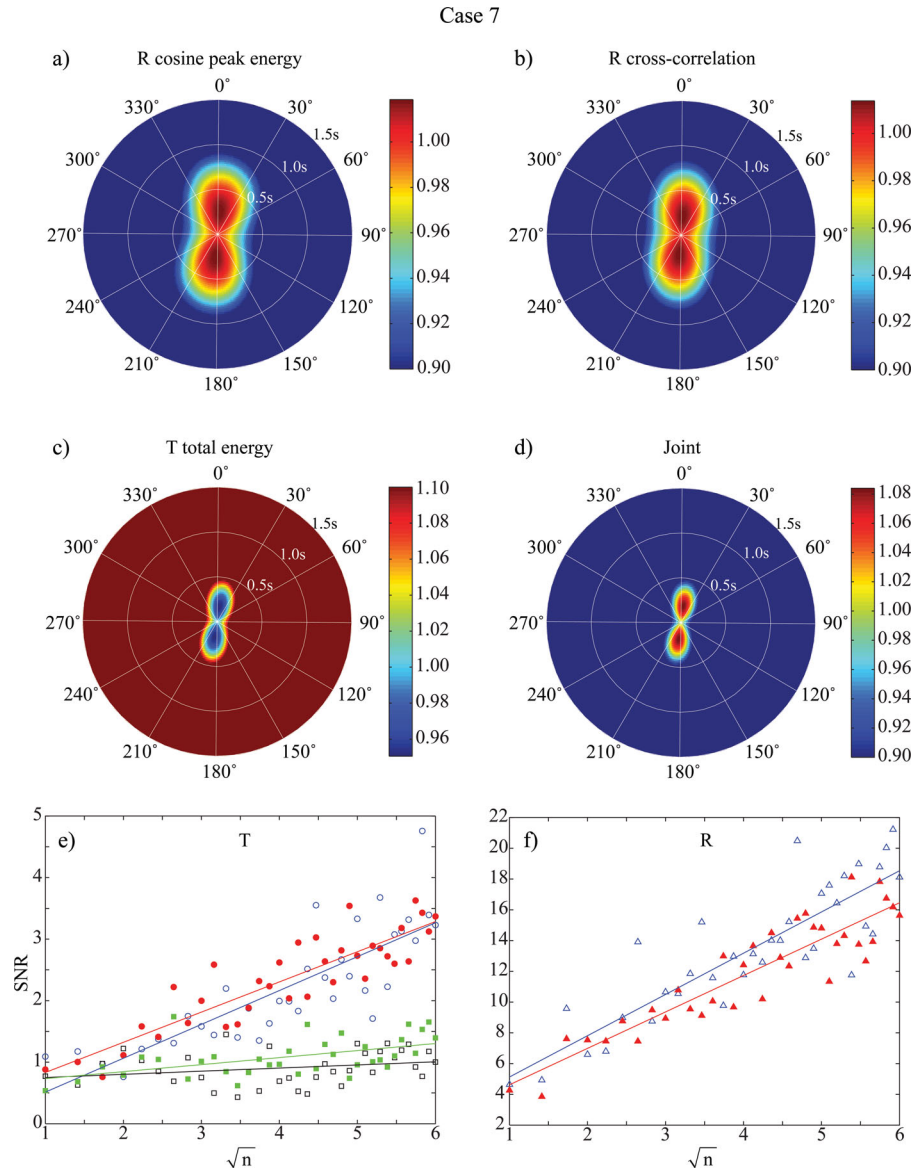


Figure 10. Results from test case 7. Same as Fig. 9 except that the backazimuths of the synthetic receiver functions are limited to one side (backazimuth 0 – 175°). Note the relatively large apparent splitting times (~ 0.2 s) estimated with the IOFs (a–c) and JOF (d). However, the maximum value of the JOF is low and the SNRT analysis also indicates little anisotropy in the data. Thus the estimated splitting parameters here are not considered to be reliable.

accurately recover the input crustal anisotropy ($\varphi = 0^\circ$, $\delta t = 0.50$ s; Figs 3a–c). The maximum amplitude of the JOF is 10.372, which is a strong evidence for the presence of seismic anisotropy in the data.

At 30 per cent noise level (case 2 in Table 2), the three IOFs are shown in Figs 4(a)–(c) and the measured splitting parameters are ($\varphi = 1^\circ$, $\delta t = 0.64$ s) for cosine moveout correction, ($\varphi = 2^\circ$, $\delta t = 0.54$ s) for R cc maximization and ($\varphi = 3^\circ$, $\delta t = 0.44$ s) for T energy minimization, respectively. The JOF is shown in Fig. 4(d), which shows a maximum at ($\varphi = 3^\circ$, $\delta t = 0.48$ s). The delay time here is slightly closer to the input value. The maximum amplitude of the joint measurement is 1.866, suggesting that the observed anisotropy is significant. The SNRT with the T receiver functions indicates that σ_{N2} (stacked after a correction of waveform polarity) increases linearly with $N^{1/2}$ (open circle in Fig. 4e) although σ_{N1} (stacked without a correction of waveform polarity)

remains nearly flat across the whole range of $N^{1/2}$ (open squares in Fig. 4e). On the other hand, once anisotropy is removed, the T receiver functions are composed mainly of random noise, leading to a flat distribution of σ_{N3} (with a polarity correction, filled circles in Fig. 4e) and σ_{N4} (without a polarity correction, filled squares in Fig. 4e). The SNRT with the R receiver function data are shown in Fig. 4(f). A correction of crustal anisotropy also seems to result in a more constructive stacking, leading to a higher SNR ($\sigma_{N6} > \sigma_{N5}$). The results from the SNRT analysis here, together with the relative large maximum amplitude shown in the joint image, indicate a clear influence of seismic anisotropy on the receiver function data.

At 60 per cent noise level (case 3 in Table 2), the three individual measurements are ($\varphi = -10^\circ$, $\delta t = 0.46$ s), ($\varphi = -11^\circ$, $\delta t = 0.46$ s) and ($\varphi = 0^\circ$, $\delta t = 0.58$ s; Figs 5a–c); the first two had a larger deviation from the input fast direction ($\varphi = 0^\circ$). The joint solution of

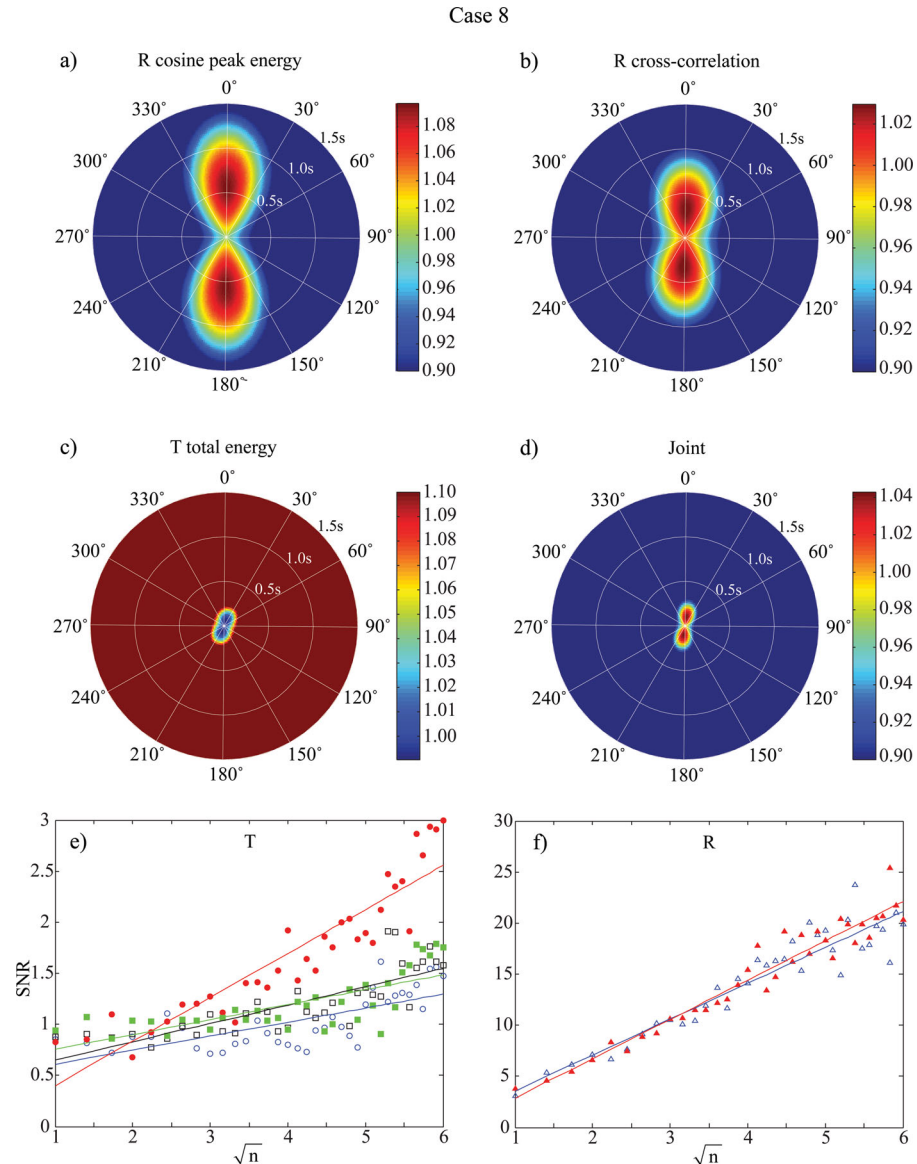


Figure 11. Results from test case 8. Same as Fig. 4 except that the synthetic receiver functions were calculated using the one-layered laterally varying velocity model, M4 (Table 1), with 30 per cent white noise. Note that the IOF corresponding to the cosine moveout correction shows large splitting time. On the other hand, the JOF has a low maximum value and the SNRT analysis also indicates no significant anisotropy in the data. Thus the proposed integrated analysis here can also resolve seismic anisotropy from heterogeneous structure.

the splitting parameters is $\varphi = -4^\circ$ and $\delta t = 0.50$ s, closer to the true values (Fig. 5d). The maximum amplitude of the joint measurement is 1.353, indicating that the anisotropy-induced signature in the data is significant. The SNRT analyses with T and R receiver functions are shown in Figs 5(e) and (f), respectively. Both show the diagnostic features of crustal anisotropy, as discussed in the test case 2.

In test case 4, we generated synthetic receiver functions with a more realistic backazimuthal coverage (here we use the same one as observed at a permanent seismic station, XJ.YCH) and a noise level of 30 per cent. The analysed results are shown in Fig. 6, which are ($\varphi = 0^\circ$, $\delta t = 0.50$ s), ($\varphi = 1^\circ$, $\delta t = 0.50$ s), ($\varphi = 3^\circ$, $\delta t = 0.48$ s) and ($\varphi = 3^\circ$, $\delta t = 0.48$ s). The maximum value of JOF, the indicator of seismic anisotropy, is also at high level, 1.781. The SNRT analysis also performed reasonably well. SNR measured from stacked receiver functions with a polarity correction, σ_{N2} , shows a steady increase with $N^{1/2}$ (open circle in Fig. 6e). Note that we used 200 receiver function pairs in this test case, thus we can confirm the linear growth of σ_{N2} up to $N^{1/2} = 14$, while in the previous three tests with a full backazimuthal coverage, we

used only 36 receiver functions, yielding a maximum of $N^{1/2} = 6$. We also noticed that the SNR computed from the original T receiver functions without a polarity correction, σ_{N1} , showing a slight increase with $N^{1/2}$ (open squares in Fig. 6e). This probably can be attributed to the uneven distribution in backazimuth of the data. The uneven distribution caused an unbalanced stacking. On the other hand, σ_{N3} computed from stacking of anisotropy-removed receiver functions with a polarity correction slightly increases. We speculate that corrections with seismic anisotropy and waveform polarity might have introduced coherent noise to the T receiver functions, for example, a projection of signals onto the R components.

We also test the performance of the joint analysis on an isotropic medium (test case 5 in Table 2). Results from individual measurement are shown in Figs 7(a)–(c). The estimated fast direction and splitting times are ($\varphi = -10^\circ$, $\delta t = 0.06$ s), ($\varphi = -15^\circ$, $\delta t = 0.08$ s) and ($\varphi = -42^\circ$, $\delta t = 0.12$ s). The joint estimate is ($\varphi = -40^\circ$, $\delta t = 0.10$ s), which seems to rely heavily on the T energy estimator. The maximum amplitude of joint measurement, which we

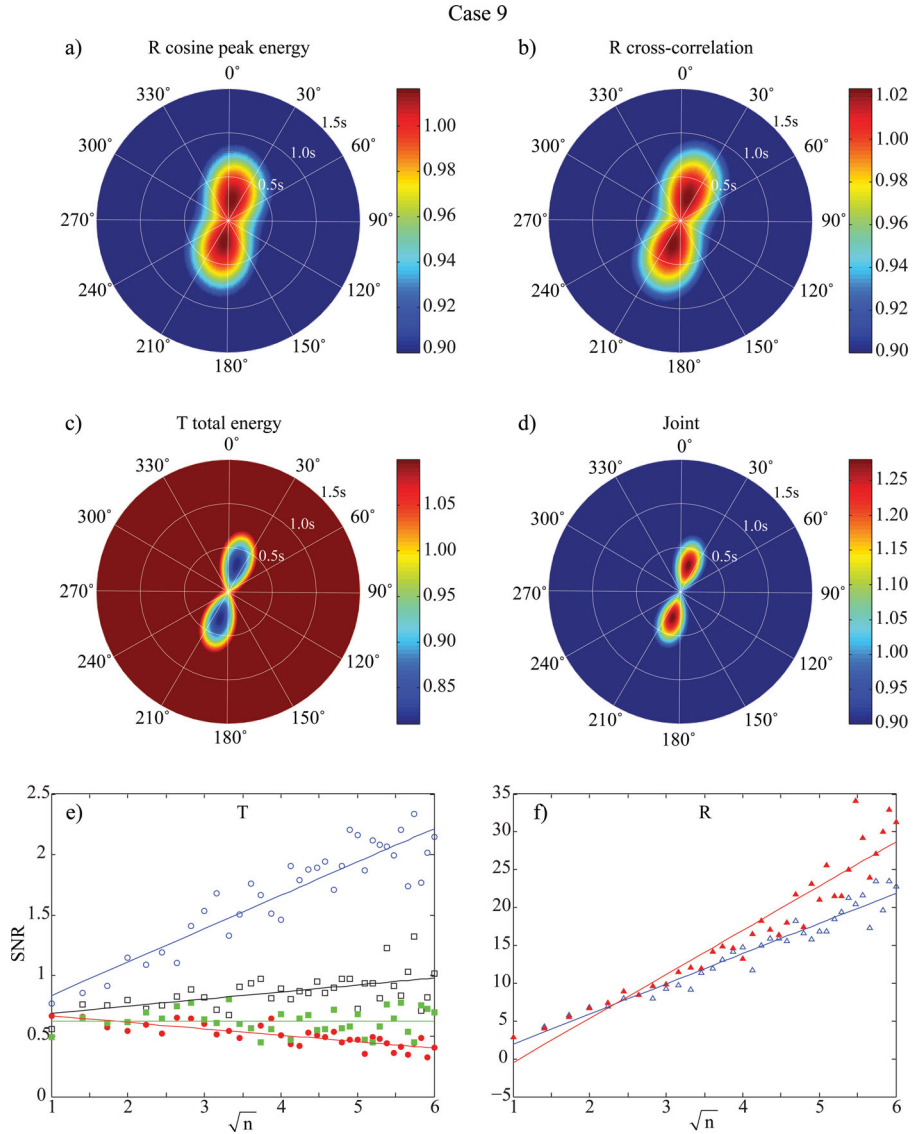


Figure 12. Results from test case 9. Same as Fig. 4 except that the synthetic receiver functions were calculated using the two-layered anisotropic model, M5 (Table 1), with 30 per cent white noise. The JOF shows a large maximum value and the SNRT also indicates the presence of seismic anisotropy in the data.

used as an indicator of anisotropy, is only 1.034, suggesting that there is little or no evidence of seismic anisotropy in the data. This is also consistent with the SNRT results. We observed no significant increase of σ_{N2} with $N^{1/2}$ from the stacking of the T receiver functions (open squares in Fig. 7e) and no substantial difference between σ_{N6} and σ_{N5} with the stacks of the R receiver functions (Fig. 7f).

Besides crustal anisotropy, a dipping Moho can also generate P_s conversion in the T component and cause backazimuthal variations in the R and T receiver functions (Figs 8a and b). The dominant variations, however, follow the $\cos\theta$ pattern, where θ is the backazimuth, in contrast to the $\cos 2\theta$ change seen from anisotropic data (e.g. Frederiksen & Bostock 2000; Shiomi & Park 2008; Bianchi *et al.* 2010). Shiomi & Park (2008) and Bianchi *et al.* (2010) noticed the above features and proposed a harmonic analysis to extract the dipping and anisotropy structure, respectively, from receiver function data. They found that it is possible to separate the two even

with the amplitude variation shown on the R and T receiver functions when a full range of backazimuthal data is available. We also performed the synthetic tests with a dipping Moho (M3 in Table 1) to see how well the isotropic crust is constrained with different coverage in backazimuth.

In test case 6, we first used a full backazimuth to constrain azimuthal anisotropy in the crust. We generated receiver functions with an isotropic crustal layer underlain by 10° dipping Moho. We added 30 per cent white noise in computing synthetic receiver functions. The IOFs computed from these receiver functions are shown in Figs 9(a)–(c) and the measured fast direction and splitting time are ($\varphi = 37^\circ$, $\delta t = 0.06$ s), ($\varphi = 12^\circ$, $\delta t = 0.08$ s) and ($\varphi = -41^\circ$, $\delta t = 0.06$ s). The JOF is shown in Fig. 9(d) and shows an apparent anisotropy of $\varphi = -27^\circ$ and $\delta t = 0.04$ s. The maximum amplitude of the joint image, however, is only 1.003, suggesting that anisotropy in the data is insignificant. The SNRT analysis applied to the T receiver functions shown in Fig. 9(e) indicates that the SNR

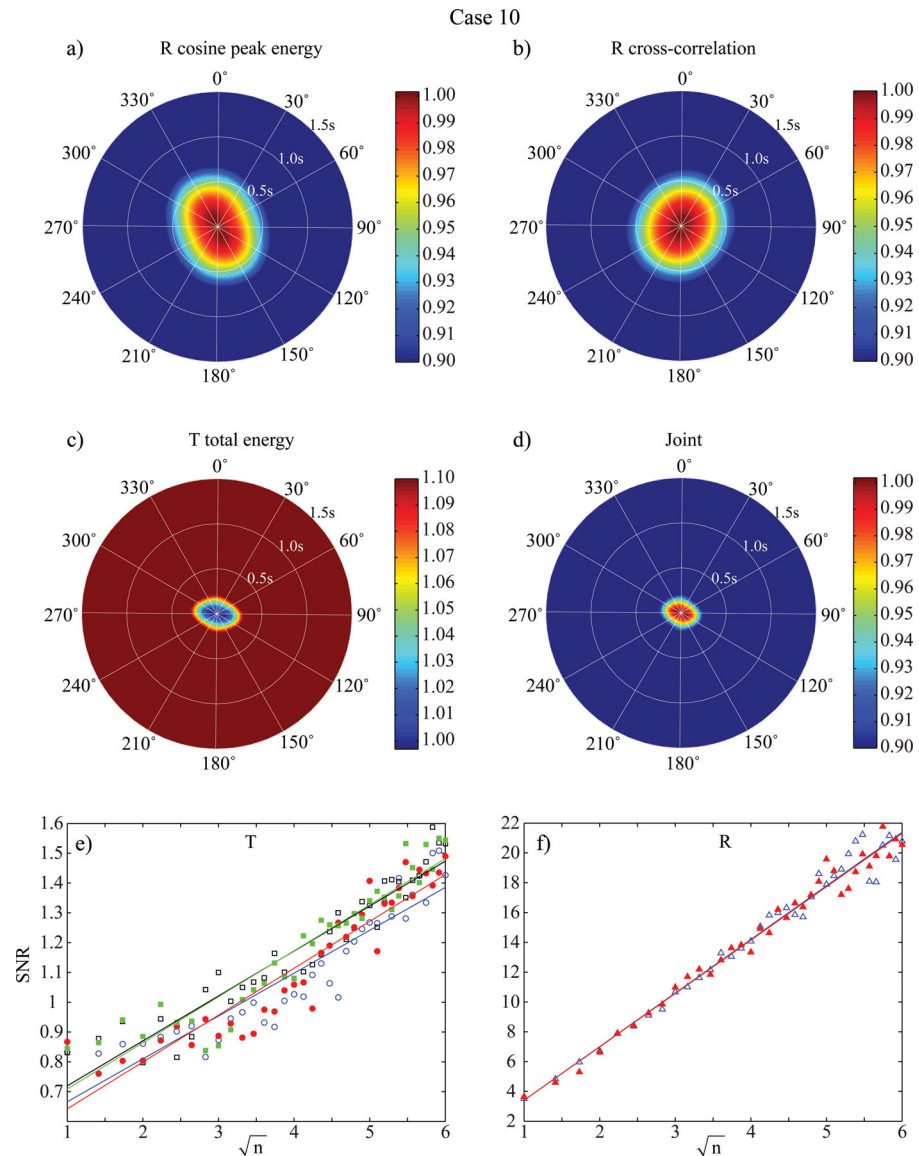


Figure 13. Results from test case 10. Same as Fig. 4 except that the synthetic receiver functions were calculated using the anisotropic upper-mantle model, M6 (Table 1), with 30 per cent white noise. Note that the low maximum value of the JOF shown in (d). The SNRT analysis also indicates no presence of crustal anisotropy in the data.

based on stacks with a polarity correction, σ_{N2} , did increase with $N^{1/2}$, but have no significant difference compared to the other three indices (σ_{N1} , σ_{N3} and σ_{N4}). This suggests that the no significant anisotropic signals exist on the T component. The SNRT with R receiver function also shows no substantial difference in SNR computed from stacks before or after the correction of seismic anisotropy (Fig. 9f).

Although the joint analysis here appears to be able to separate anisotropy from dipping structure given a good coverage in backazimuth, we further tested whether this is true even under conditions when backazimuth coverage of the data is limited. In test case 7, we generated synthetics with a one side backazimuthal distribution and 30 per cent white noise. All the individual measurements show a relatively large apparent splitting time of $\delta t = 0.24$, 0.20 and 0.16 s, with a fast direction of $\varphi = 8^\circ$, 5° and 9° , respectively (Figs 10a–c). The joint measurement also yielded an apparent anisotropy with $\varphi = 9^\circ$ and $\delta t = 0.18$ s (Fig. 10d). The maximum amplitude of joint measurement is, however, as low as 1.084, which is consistent with the results of the SNRT analysis. Both indicate that the observed anisotropy is not a reliable feature in the data.

In test case 8, we tested how lateral heterogeneities in crustal velocity structure affect our anisotropy measurements. As shown in Fig. 1, seismic anisotropy introduce a four-lobed variation in the peak P_s arrival time and P_s polarity on the R and T receiver functions, respectively. To mimic the anisotropic effect, we set up a model with two velocity values alternating from quadrant-to-quadrant (M4 in Table 1). Using this model we generated synthetic receiver function with 30 per cent white noise. We then computed the IOFs and JOF with the corresponding R and T receiver functions, which are shown in Fig. 11. The maximum of the individual functions occurred at $(\varphi = 0^\circ, \delta t = 0.52$ s), $(\varphi = 2^\circ, \delta t = 0.32$ s) and $(\varphi = 20^\circ, \delta t = 0.06$ s), respectively, and the joint function shows a maximum at $(\varphi = 12^\circ, \delta t = 0.10$ s). The maximum amplitude of the JOF is only 1.043, suggesting that there is little or no seismic

anisotropy in the data. The SNRT analyses with T (Fig. 11e) and R (Fig. 11f) also show no evidence of seismic anisotropy in the data, suggesting the observed small amount of anisotropy might be an artefact.

In test case 9, we used a model consisting of two anisotropic layers with different fast polarization directions (M5 in Table 1). The individual measurements show an apparent anisotropy with fast direction $\varphi = 11^\circ$, 16° and 16° and splitting time $\delta t = 0.22$, 0.28 and 0.32 s (Figs 12a–c), respectively. The joint measurement gave more or less the same estimate with a fast direction of $\varphi = 16^\circ$ and a delay time of $\delta t = 0.30$ s (Fig. 12d). The apparent anisotropy is consistent with a vector summation of the two splitting vectors computed from the upper and lower crust. Both the maximum amplitude of the JOF (1.280) and the SNRT analysis with the T (Fig. 12e) and R (Fig. 12f) receiver functions indicate the presence of seismic anisotropy in the data.

The last model we tested has a 50-km-thick isotropic crust underlain by an anisotropic mantle (M6 in Table 1), in which case, the synthetics show clear P_s conversions in the transverse component. The corresponding R and T receiver functions also exhibit a $\cos 2\theta$ variation along the backazimuthal direction, θ (Figs 8c and d). There is, however, no clear evidence of backazimuthal variation in the P_s arrival time on the R component, as shown in Fig. 1(a). We also noticed that the waveforms of the P_s conversion are rather similar between the R and T receiver functions, in contrast to those computed from anisotropic models. In the latter case, the T component is approximately proportional to the time derivative of the R component (Figs 1a and b). The $\cos 2\theta$ backazimuthal variation could be easily misinterpreted as crustal anisotropy if an analysis only relies on the amplitude of R and T receiver functions. In test case 10, we applied the joint analysis to the synthetic receiver functions computed from model M6. The individual measurements show an apparent anisotropy with fast direction $\varphi = 146^\circ$, 22° and 101° and a splitting time $\delta t = 0.08$, 0.02 and 0.04 s (Figs 13a–c), respectively.

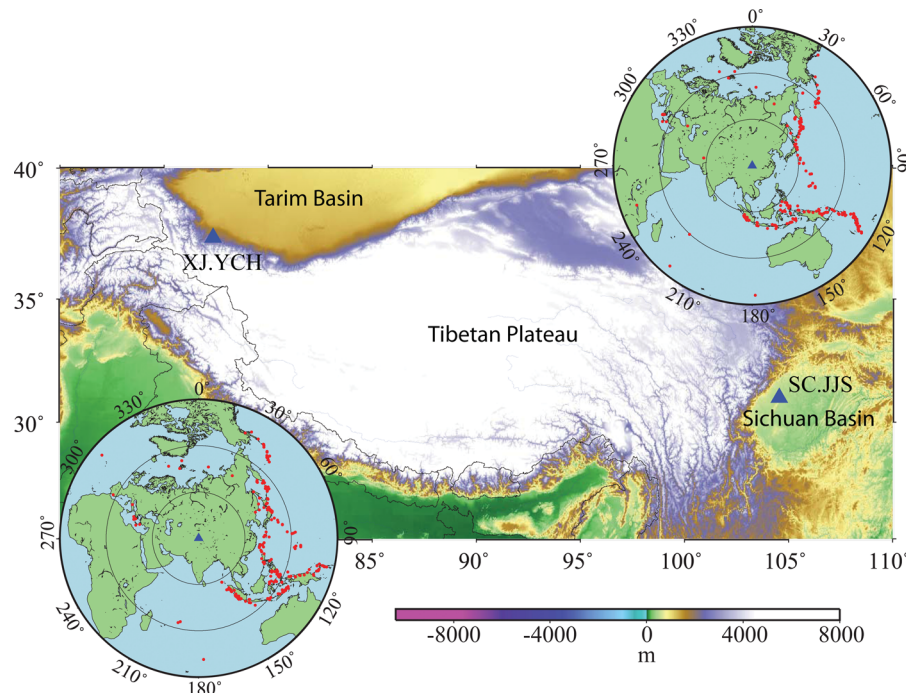


Figure 14. Map showing the geographic locations of two seismic stations XJ.YCH and SC.JJS used in this study. Insets show the backazimuthal distribution of the teleseismic events at epicentral distances between 30° and 90° with an $M_w \geq 5.8$.

The joint measurement gave a fast direction of $\varphi = 101^\circ$ and a delay time of $\delta t = 0.02$ s (Fig. 13d). The maximum value of the JOF is as low as 1.002. This is consistent with the SNRT analysis (Figs 13e and f). Both show no evidence for crustal anisotropy.

Results of the joint measurement of the 10 cases are summarized in Table 2. In all the cases, the maximum value of the JOF can be combined with the SNRT analysis to determine the existence of seismic anisotropy in the R and T receiver function data. If seismic anisotropy is required to explain the data, we can compute the three IOFs and their combination to obtain relatively robust estimate of crustal anisotropy in the data.

4 DATA EXAMPLES

We have applied this integrated technique to receiver function data recorded at two broadband stations, XJ.YCH and SC.JJS, in western China. Both stations belong to the permanent network of the China Earthquake Administration. XJ.YCH (77.361E, 37.390N) is located at the northern edge of the Tibetan plateau near the southwest corner of the Tarim Basin, while SC.JJS (104.546E, 31.005N) is situated inside the Sichuan basin east to the Tibetan plateau (Fig. 14). We generated receiver functions from records of earthquakes that occurred at epicentral distances of 30° – 90° between 2007 July and 2010 July with $M_w \geq 5.8$. The 3-yr data set provided a good backazimuthal coverage (Fig. 14 insets), which is essential for a robust estimate of crustal anisotropy.

Fig. 15 shows the selected receiver functions recorded at station XJ.YCH plotted as a function of backazimuth. The slightly negative moveout of the Moho P_s converted phase was corrected as if all the receiver functions were received at an epicentral distance of 60° and a focal depth of 0 km. The Moho converted P_s phase on the R receiver functions appears to exhibit a four-lobed variation pattern in arrival time (Fig. 15a). It also seems that there are polarity changes in the P_s waveform on the T receiver functions (Fig. 15b). As mentioned above, these observed features suggest the existence of seismic anisotropy in the data.

We computed the three IOFs and the JOF using the 239 receiver function data (Fig. 16). The crustal anisotropy estimated from the first two IOFs show good agreement, with a fast direction of $\varphi = \sim 105^\circ$ and a splitting time of $\delta t = \sim 0.65$ s. The fast direction measured with the T energy minimization is $\varphi = 125^\circ$, approximately 20° larger than the R measurements, with a delay time of $\delta t = 0.54$ s. The JOF reaches its maximum at ($\varphi = 110^\circ$, $\delta t = 0.58$ s) with a maximum value of 1.743 (Fig. 16d). The SNR measured from stacked T receiver functions with a polarity correction, σ_{N2} , exhibited a steady increase with $N^{1/2}$, although those measured with other stacks (σ_{N1} , σ_{N3} and σ_{N4}) show a very little increase with increasing N (Fig. 16e). The SNR computed from stacks of R receiver functions after the removal of seismic anisotropy is also slightly higher than that calculated from the original R receiver functions. Both the maximum amplitude and the SNRT analysis indicate that the crust beneath this station is significantly anisotropic. Solid and dashed lines in Figs 15(c) and (d) represent stacked R and T (with changes in polarity) receiver functions before and after the correction. The amplitude of the Moho P_s conversion signal is enhanced on the stacked R receiver function but reduced on the stacked T receiver function after correction.

Levin *et al.* (2008) analysed SKS/PKS and receiver function data recorded by a temporary array deployed in the area near XJ.YCH for 6 months by a Sino-French group. XJ.YCH is closest to their station 108 (in fig. 2 of Levin *et al.* 2008), where no measure-

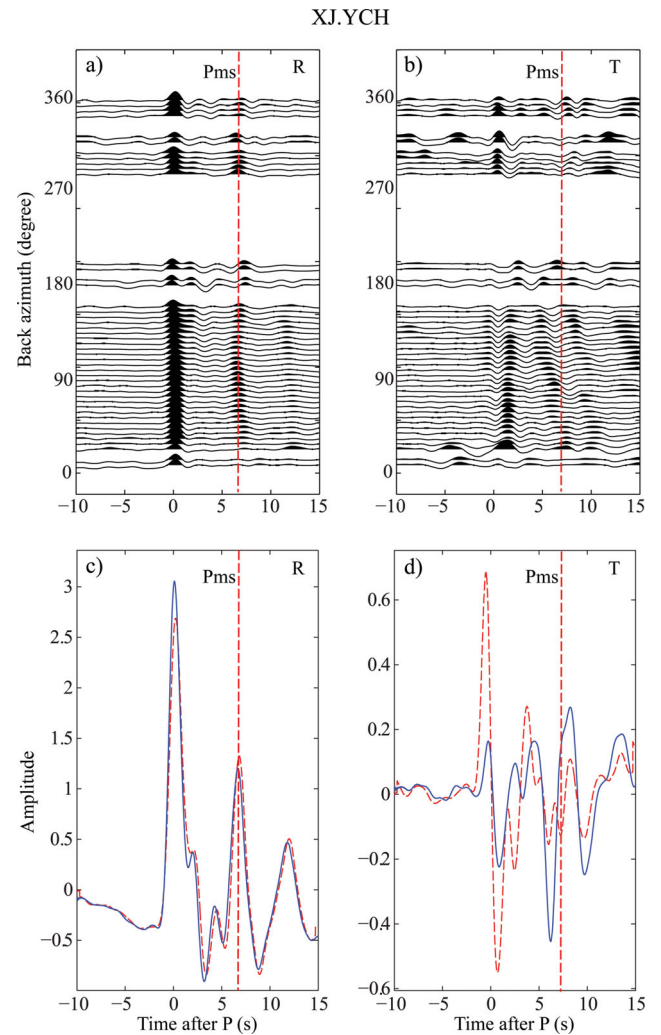


Figure 15. R (a) and T (b) receiver functions recorded at station XJ.YCH are plotted as a function of backazimuth (binned every 10°). The T receiver functions shown in (b) are magnified by a factor of 2. The vertical dashed line indicates the average arrival time of the Moho P_s converted phase. The stacked R receiver functions (c) and T receiver functions (d) before/after corrections of seismic anisotropy determined by the JOF are shown in solid/dashed lines, respectively. Note that the P_s energy on the stacks of polarity-corrected T receiver functions is significantly reduced after the correction.

ment of crustal anisotropy is available. We thus compare our results with their measurements at stations 104 and 116, which are located approximately 50 km north and 110 km south of XJ.YCH, respectively. The SKS/PKS splitting data recorded at station 116 can be best explained by a one-layer anisotropic model of ($\varphi = 108^\circ$, $\delta t = 1.0$ s) or a two-layer model of ($\varphi = 112$ – 120° , $\delta t = 0.8$ – 1.6 s) and ($\varphi = 36$ – 86° , $\delta t = 0.4$ – 0.6 s) for the upper and lower layer, respectively. The best fitting model of receiver function data collected at station 104 has a ~ 10 km strong anisotropic layer above the Moho with a fast direction of 130° , which is consistent with the estimate of the third IOF and $\sim 20^\circ$ larger than the joint solution. The fast polarization direction observed here is roughly parallel to the Altyn Tagh fault in this area, along the direction of maximum horizontal tensile stress. We thus speculated that mineral alignment in the lower crust is likely responsible for the observed seismic anisotropy.

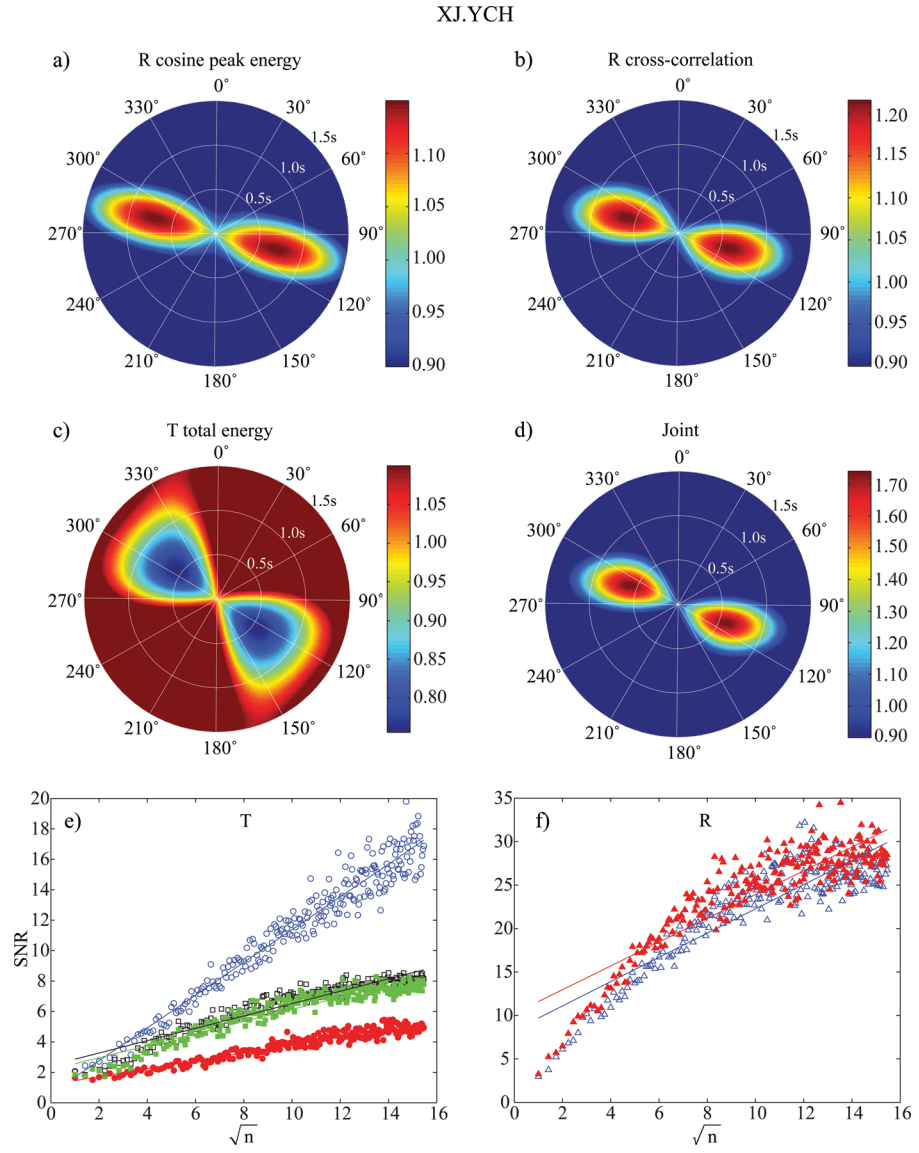


Figure 16. Results obtained at station XJ.YCH, which are plotted similarly to Fig. 4. The three IOFs and the JOF are shown in (a), (b), (c) and (d), respectively. Results of the SNRT analysis based on the T and R receiver functions are shown in (e) and (f), respectively. Note that in (e), only stacks from polarity-corrected T receiver functions (open circles) show a steady increase of SNR with increasing $N^{1/2}$, although the other stacks exhibited little to no dependence on N . Also stacks of R receiver functions after the correction of anisotropy show a slightly higher SNR than those from the original radial data.

We have a total of 210 selected receiver functions recorded at the station SC.JJS inside the Sichuan basin. We first corrected the time-distance moveout of the P_s phase in the receiver functions then plotted in the order of backazimuth (Fig. 17). We found no clear evidence of any systematic variations in P_s waveform and arrival time with respect to backazimuth. The calculated three IOFs are shown in Figs 18(a)–(c) and the JOF is shown in Fig. 18(d). The estimated crustal anisotropy from the two R and T measurements is ($\varphi = 149^\circ$, $\delta t = 0.08$ s), ($\varphi = 143^\circ$, $\delta t = 0.02$ s) and ($\varphi = 75^\circ$, $\delta t = 0.06$ s), respectively. The JOF reaches its maximum at ($\varphi = 79^\circ$, $\delta t = 0.06$ s) with a maximum value of 1.028. The SNRT analysis results with the T and R receiver functions are shown in Figs 18(e) and (f), respectively. The calculated SNRs from receiver functions with different types of stacking didn't show any evidence of seismic anisotropy in the data. The insignificance of seismic anisotropy in the data can also be shown by comparing the stacked receiver functions before and after the correction of seismic anisotropy. Solid and

dashed lines in Figs 17(c) and (d) represent the stacked R and T receiver functions before and after the correction. Waveforms within the Moho P_s arrival time window on both components show no significant changes after the removal of seismic anisotropy. The station is located within the Sichuan basin where very little deformation is observed at surface. Our observation here is that the crust beneath SC.JJS has a rather isotropic velocity structure thus is consistent with surface observation and may indicate there is little crust-scale deformation inside the basin.

5 DISCUSSION AND CONCLUSIONS

The P -to- S converted phase at the Moho boundary is an ideal phase to study crustal anisotropy. Receiver functions, however, have not been extensively used in measuring seismic anisotropy in crust, because the P_s conversion is a very weak signal. Measurements

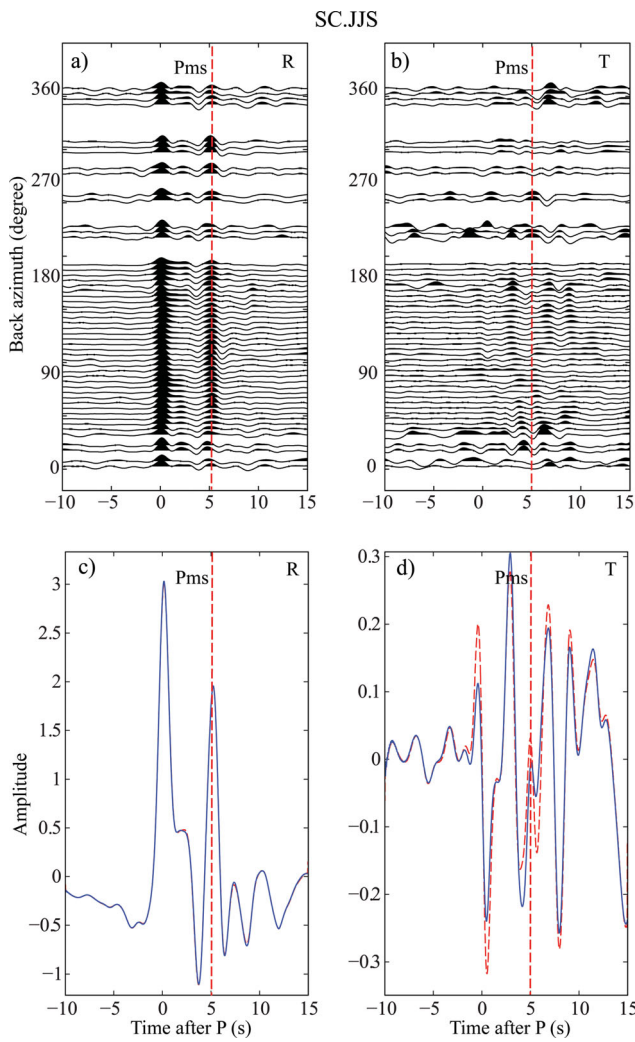


Figure 17. R (a) and T (b) receiver functions recorded at station SC.JJS are shown as a function as backazimuth (binned every 10°). The T receiver functions shown in (b) are magnified by a factor of 2. The vertical dashed line indicates the average arrival time of the Moho P_s converted phase. The stacked R receiver functions (c) and T receiver functions (d) before/after corrections of seismic anisotropy determined by the JOF are shown in solid/dashed lines, respectively. Note that the stacked P_s waveform after correction of seismic anisotropy remains almost the same on both components, suggesting crustal anisotropy is insignificant in the data.

with individual receiver function data can introduce large errors and even lead to wrong estimates of crustal anisotropy. We found that a joint analysis of all the receiver functions recorded at a single seismic station is a preferred approach.

We proposed three different ways to estimate seismic anisotropy in this study. As R receiver functions always have better SNRs than T receiver functions, it is conceivable to develop method to rely solely on R receiver functions to estimate crustal anisotropy. Our first method searches a pair of $(\varphi, \delta t)$ that maximize the stacked P_s amplitude after a cosine moveout correction in the P_s arrival time. As a dipping Moho and velocity heterogeneities in crust could also cause backazimuthal variations in P_s arrival time, we found this method has little resolution of anisotropy from the above two inhomogeneous structures, especially when the backazimuth coverage is poor (test cases 7 and 8, Figs 10 and 11). Our second and third methods make a full correction of seismic anisotropy on R and T receiver functions. They track the effects of the correction on the

R cc and T energy, respectively. Between the two methods, the minimization of T energy appears to better recover the input models, although it could misinterpret dipping Moho structure with crustal anisotropy when coverage in backazimuth is poor (case 7, Fig. 10).

We equally weighted the three individual measurements when computing the JOF. As shown in the Appendix, the significances of maximums of the three IOFs are proportional to δt^2 , thus we have used it as the indicator of seismic anisotropy in the data. We also noticed that the maximum value of the T objective function is larger than those of the R estimators when noise level is low [comparing (A7) with (A2b) and (A4)]. As the JOF was computed by a geometric mean of the three objectives functions, we found that the joint estimates of seismic anisotropy tend to agree better with those of the T estimator in our tests (Figs 3–13). On the other hand, our synthetic tests indicated that measurements from the three methods are generally consistent with each other, thus the selection of different weights appears to have little effects on the joint estimates.

Besides the maximum value of the JOF, we also found that the SNRT analysis can be used to verify whether there is significant seismic anisotropy in the receiver function data. The SNRT analyses of the anisotropic models show that SNR computed from stacks of T receiver functions after the waveform polarity been corrected, σ_{N2} linearly increases with $N^{1/2}$ and stacks of R receiver functions after removal of anisotropy always have higher SNR than those from original data ($\sigma_{N6} > \sigma_{N5}$). The three individual plus the joint measurements of seismic anisotropy and the SNRT analysis should be considered as one integrated technique which provides a robust and reliable way for identifying and estimating crustal anisotropy with receiver function data.

The joint analysis is designed to constrain a special type of seismic anisotropy in Earth's crust, azimuthal anisotropy using receiver function data. When radially polarized S waves propagate through such an anisotropic crust, their energy splits and part of it is projected onto the transverse component. The birefringent T waveforms are proportional to the time derivative of those on the R component. In addition, the amplitude and the arrival time of the birefringent S waves exhibit a four-lobe variation pattern along the backazimuth direction. We found that these two unique features of azimuthal anisotropy provide a strong base for resolving it from other heterogeneous structures, such as velocity heterogeneities in the crust and a tilted CMB, which were demonstrated in our synthetic tests.

It should be noted that the anisotropic structure within Earth's crust is likely to be more complicated. In addition to azimuthal anisotropy with a horizontal symmetry axis, there are other types of anisotropic structures that are not addressed in this study. Many studies (e.g. Levin *et al.* 2008) have shown that an inclination of the symmetry axis leads to a mix of $\cos \theta$ and $\cos 2\theta$ directional variation. If this is the case, then our measurements can be considered as the horizontal projection of the 3-D anisotropic structure. Meanwhile, P -wave anisotropy in the crust can also cause directional variations in receiver function data by affecting the travel-time of the primary P wave. The induced backazimuthal variation is, however, different from the $\cos 2\theta$ change caused by azimuthal anisotropy and thus should not be misinterpreted by the joint analysis. It should also be noted that the estimated seismic anisotropy here reflects the integrated anisotropic structure across the entire crust, as the joint analysis was only applied to the Moho P_s conversion phase. Although we have used homogenous anisotropic models in our synthetic tests, the analysis can be used to estimate azimuthal anisotropy that has an uneven distribution with depth.

We applied the integrated analysis to two permanent stations in western China. The station located in the northern edge of the

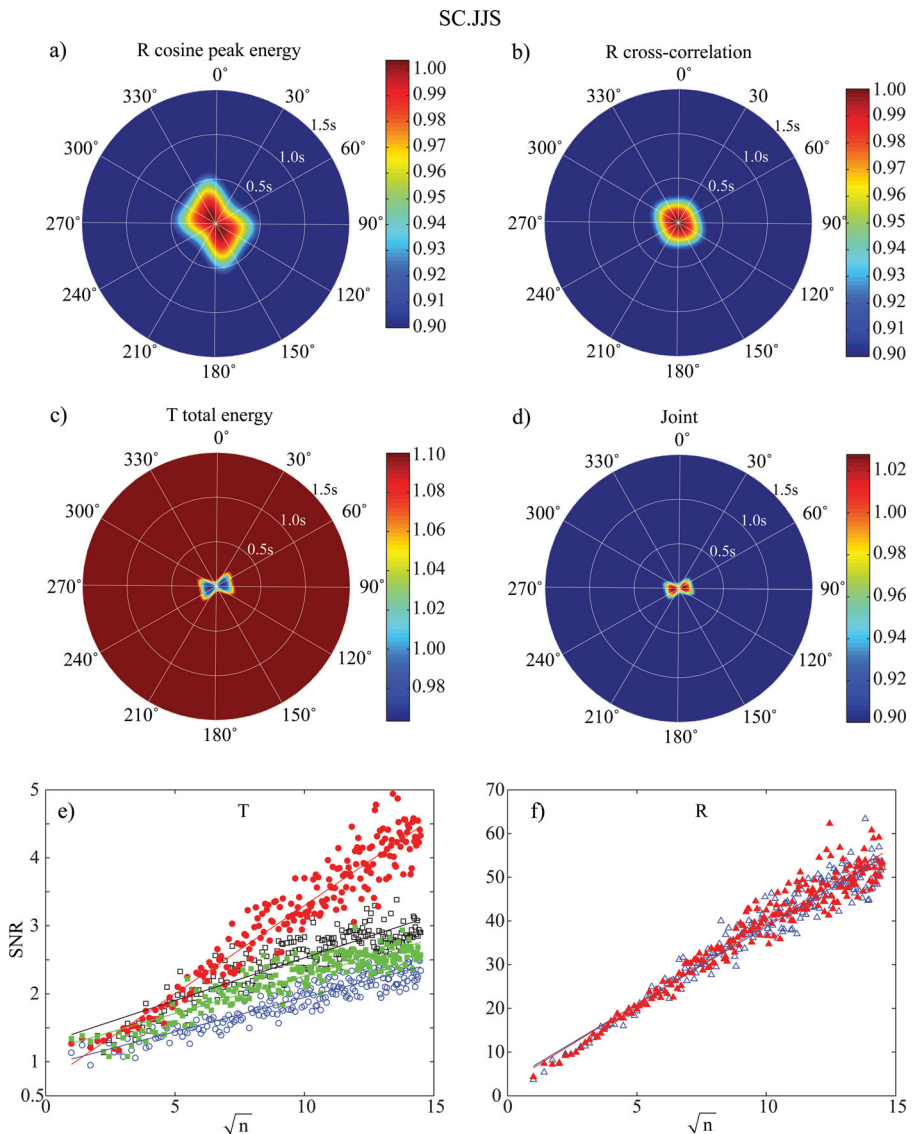


Figure 18. Results obtained at station SC.JJS, which are plotted similarly to Fig. 4. The three IOFs and the JOF are shown in (a), (b), (c) and (d), respectively. Results of the SNRT analysis based on the T and R receiver functions are shown in (e) and (f), respectively. Note that open circles in (e) show no significant increase with increasing $N^{1/2}$ and the open and filled triangles in (f) mix with each other, suggesting that there is a little to no anisotropy in the data.

Tibetan plateau shows significant seismic anisotropy within the crust while the other one located inside the Sichuan basin exhibited little to no seismic anisotropy. The results here agree with the surface deformation and probably reflect deformation occurring within the lower crust. The relative large splitting time ($\delta t = 0.5$ s) observed in the Tibetan crust suggests that crustal contribution needs to be considered in interpreting SKS measurement in regions like Tibet where a thick crust is present. The same analysis can be applied to any stations with relatively good backazimuthal coverage to study crustal anisotropy and to understand crustal deformation.

ACKNOWLEDGMENTS

We would like to thank the Data Management Center of the China Earthquake Administration for providing seismic data, and Dr Yuan Gao at the Institute of Earthquake Science, China Earthquake Ad-

ministration for discussion. We would also like to thank Drs Vadim Levin and Andrew Frederiksen for their critical and constructive comments, which significantly improved the quality of this paper. This work was supported by NSF grant EAR-0748455.

REFERENCES

- Ammon, C.J., 1991. The isolation of receiver effects from teleseismic p waveforms. *Bull. seism. Soc. Am.*, **81**, 2504–2510.
- Bianchi, I., Park, J., Piana Agostinetti, N. & Levin, V., 2010. Mapping seismic anisotropy using harmonic decomposition of receiver functions: an application to Northern Apennines, Italy. *J. geophys. Res.*, **115**, B12317, doi:10.1029/2009JB007061.
- Bowman, J.R. & Ando, M., 1987. Shear-wave splitting in the upper-mantle wedge above the Tonga subduction zone. *Geophys. J. R. astr. Soc.*, **88**, 25–41.
- Clark, M.K. & Royden, L.H., 2000. Topographic ooze: building the eastern margin of Tibet by lower crustal flow. *Geology*, **28**, 703–706.

- Clayton, R.W. & Wiggins, R.A., 1976. Source shape estimation and deconvolution of teleseismic body waves. *Geophys. J. R. astr. Soc.*, **47**, 151–177.
- Crampin, S., 1987. Geological and industrial implications of extensive dilatancy anisotropy. *Nature*, **328**, 491–496.
- Crampin, S. & Chastin, S., 2003. A review of shear wave splitting in the crack-critical crust. *Geophys. J. Int.*, **155**, 221–240.
- Crampin, S. & Lovell, J.H., 1991. A decade of shear-wave splitting in the Earth's crust: what does it mean? What use can we make of it? and what should we do next?. *Geophys. J. Int.*, **107**, 387–407.
- Frederiksen, A.W. & Bostock, M.G., 2000. Modelling teleseismic waves in dipping anisotropic structures. *Geophys. J. Int.*, **141**, 401–412.
- Iidaka, T. & Niu, F., 2001. Mantle and crust anisotropy in the eastern China region as inferred from waveform splitting of SKS and PpSms. *Earth, Planets Space*, **53**, 159–168.
- Kaneshima, S., 1990. Origin of crustal anisotropy: shear wave splitting studies in Japan. *J. geophys. Res.*, **95**, 11 121–11 133.
- Kennett, B.L.N. & Engdahl, E.R., 1991. Traveltimes for global earthquake location and phase identification. *Geophys. J. Int.*, **105**, 429–465.
- Levin, V. & Park, J., 1997. P-SH conversions in a flat-layered medium with anisotropy of arbitrary orientation. *Geophys. J. Int.*, **131**, 253–266.
- Levin, V., Roecker S., Graham, P. & Hosseini, A., 2008. Seismic anisotropy indicators in Western Tibet: shear wave splitting and receiver function analysis. *Tectonophysics*, **462**, 99–108.
- Li, J. & Niu, F., 2010. Seismic anisotropy and mantle flow beneath northeast China inferred from regional seismic networks. *J. geophys. Res.*, **115**, B12 327, doi:10.1029/2010JB007470.
- Masy, J., Niu, F., Levander, A. & Schmitz M., 2011. Mantle flow beneath northwestern Venezuela: seismic evidence for a deep origin of the Mérida Andes. *Earth planet. Sci. Lett.*, **305**, 396–40, doi:10.1016/j.epsl.2011.03.024.
- McNamara, D.E. & Owens, T.J., 1993. Azimuthal shear wave velocity anisotropy in the Basin and Range Province using Moho Ps converted phases. *J. geophys. Res.*, **98**, 12 003–12 017.
- McNamara, D.E., Owens, T.J., Silver, P.G., & Wu, F.T., 1994. Shear wave anisotropy beneath the Tibetan Plateau. *J. geophys. Res.*, **99**, 13 655–13 665.
- Meade, C., Silver, P.G. & Kaneshima, K., 1995. Laboratory and seismological observations of lower mantle isotropy. *Geophys. Res. Lett.*, **22**, 1293–1296.
- Nagaya, M., Oda, H., Akazawa, H. & Ishise, M., 2008. Receiver functions of seismic waves in layered anisotropic media: application to the estimate of seismic anisotropy. *Bull. seism. Soc. Am.*, **98**, 2990–3006.
- Nicolas, A. & Christensen, N.I., 1987. Formation of anisotropy in upper mantle peridotites—a review, in *Composition, Structure and Dynamics of the Lithosphere-Asthenosphere System*, pp. 111–123, eds K. Fuchs & C. Froidevaux, American Geophysical Union, Washington, DC.
- Niu, F. & Perez, A.M., 2004. Seismic anisotropy in the lower mantle: a comparison of waveform splitting of SKS and SKKS. *Geophys. Res. Lett.*, **31**, doi:10.1029/2004GL021196.
- Peng, X. & Humphreys, E.D., 1997. Moho dip and crustal anisotropy in northwestern Nevada from teleseismic receiver functions. *Bull. seism. Soc. Am.*, **87**, 745–754.
- Savage, M.K., 1998. Lower crustal anisotropy or dipping boundaries? Effects on receiver functions and a case study in New Zealand. *J. geophys. Res.*, **103**, 15 069–15 087.
- Shiomi, K. & Park, J., 2008. Structural features of the subducting slab beneath the Kii Peninsula, central Japan: seismic evidence of slab segmentation, dehydration, and anisotropy. *J. geophys. Res.*, **113**, B10318, doi:10.1029/2007JB005535.
- Silver, P.G., 1996. Seismic anisotropy beneath the continents: probing the depths of Geology. *Annu. Rev. Earth planet. Sci.*, **24**, 385–432.
- Silver, P.G. & Chan, W.W., 1991. Shear wave splitting and subcontinental mantle deformation. *J. geophys. Res.*, **96**, 16 429–16 454.
- Wolfe, C.J. & Silver, P.G., 1998. Seismic anisotropy of oceanic upper mantle: shear wave splitting methodologies and observations. *J. geophys. Res.*, **103**, 749–771.

APPENDIX: RELATIONSHIP BETWEEN THE MAXIMUM OF THE IOFS AND DELAY TIME

In this appendix, we would like to show that the maximum of the three IOFs ($I_{r\cos}(\varphi, \delta t)$, $I_{rc}(\varphi, \delta t)$ and $I_t(\varphi, \delta t)$) can be expressed as $1 + c\delta t^2$, where c is a constant, that is,

$$I_{r\cos}(\varphi, \delta t) = 1 + c_1\delta t^2; \quad I_{rc}(\varphi, \delta t) = 1 + c_2\delta t^2; \quad I_t(\varphi, \delta t) = 1/(1 + c_3\delta t^2). \quad (\text{A1})$$

To simplify the derivation of (A1), here we assume that the Moho Ps conversion wave can be approximated by a half cosine function $\cos \omega_0(t - t_0)$, where ω_0 is dominant frequency and t_0 is the isotropic arrival time of the Moho converted phase. The R receiver function at backazimuth θ can be expressed as $\cos \omega_0[t - t_0 + \frac{\delta t}{2} \cos 2(\theta - \varphi)]$, where φ is the fast polarization direction. The maximum stacking amplitude occurs at $t = t_0$ and is expected to be 1 after correction. Thus the first IOF can be computed from

$$\begin{aligned} \max\{I_{r\cos}(\varphi, \delta t)\} &= 1 \left/ \left\{ \frac{1}{2\pi} \int_0^{2\pi} \cos \left[\omega_0 \frac{\delta t}{2} \cdot \cos 2(\theta - \varphi) \right] d\theta \right\}^2 \right. \\ &\approx 1 \left/ \left\{ \frac{1}{2\pi} \int_0^{2\pi} \left\{ 1 - \frac{1}{2} \cdot \left[\frac{\omega_0 \delta t}{2} \cdot \cos 2(\theta - \varphi) \right]^2 \right\} d\theta \right\}^2 \right. \end{aligned} \quad (\text{A2a})$$

which is

$$\max\{I_{r\cos}(\varphi, \delta t)\} \approx 1 + \frac{\omega_0^2}{8} \delta t^2. \quad (\text{A2b})$$

For a pair of R receiver functions with a time shift δt_i , the cross correlation ratio after and before anisotropic correction is

$$\begin{aligned} I_{ri\,cc} &= \int_{t_0-T_0/4}^{t_0+T_0/4} \cos^2 \omega_0(t - t_0) dt / \int_{t_0-T_0/4}^{t_0+T_0/4} \cos \omega_0(t - t_0 - \delta t_i) \cos \omega_0(t - t_0 - \delta t_j) dt \\ &\approx \int_{-T_0/4}^{T_0/4} \cos^2 \omega_0 t dt / \int_{-T_0/4}^{T_0/4} \cos^2 \omega_0 t \left(1 - \frac{\omega_0^2}{2} \delta t_i^2\right) \left(1 - \frac{\omega_0^2}{2} \delta t_j^2\right) dt \\ &\approx 1 + \frac{\omega_0^2}{2} \delta t_i^2 + \frac{\omega_0^2}{2} \delta t_j^2. \end{aligned} \quad (\text{A3})$$

As $\delta t_i = \frac{\delta t}{2} \cos 2(\theta - \varphi)$, so the second IOF can be calculated by the averaging δt_i^2 over the entire range of the backazimuth:

$$\begin{aligned} \max\{I_{ri\,cc}(\varphi, \delta t)\} &= \frac{1}{2\pi} \int_0^{2\pi} \left\{ 1 + \frac{\omega_0^2}{2} \frac{\delta t^2}{4} [\cos^2 2(\theta_i - \varphi) + \cos^2 2(\theta_j - \varphi)] \right\} d\theta \\ &\approx 1 + \frac{\omega_0^2}{8} \delta t^2. \end{aligned} \quad (\text{A4})$$

For an incoming S wave with a source time function $s(t)$ and a radial polarization direction θ , the T component generated by azimuthal anisotropy is

$$\begin{aligned} T(t) &= \frac{1}{2} \left\{ s \left(t - t_0 + \frac{\delta t}{2} \right) - s \left(t - t_0 - \frac{\delta t}{2} \right) \right\} \sin(\theta - \varphi) \cos(\theta - \varphi) + n(t) \\ &= \frac{1}{2} s'(t - t_0) \delta t \sin 2(\theta - \varphi) + n(t), \end{aligned} \quad (\text{A5})$$

where $n(t)$ is random noise. If we assume $s(t) = \cos(\omega_0 t)$, then $s'(t) = -\omega_0 \sin(\omega_0 t)$. Then the T energy ratio before and after anisotropic correction is

$$\begin{aligned} I_t^{-1}(\theta) &= \int_{t_0-T_0/4}^{t_0+T_0/4} \left\{ -\frac{\omega_0}{2} \sin \omega_0(t - t_0) \delta t \sin 2(\theta - \varphi) + n(t) \right\}^2 dt / \int_{t_0-T_0/4}^{t_0+T_0/4} n^2(t) dt \\ &= 1 + \frac{\omega_0^2}{8} \delta t^2 \sin^2 2(\theta - \varphi) / \bar{E}_n, \end{aligned} \quad (\text{A6})$$

where $\bar{E}_n = \frac{2}{T_0} \int_{t_0-T_0/4}^{t_0+T_0/4} n^2(t) dt$ is the average noise energy within the Moho Ps arrival time window. Taking the average across the entire backazimuth,

$$\begin{aligned} \max\{I_t^{-1}(\varphi, \delta t)\} &= \frac{1}{2\pi} \int_0^{2\pi} \left[1 + \frac{\omega_0^2}{4} \delta t^2 \sin^2 2(\theta - \varphi) / \bar{E}_n \right] d\theta \\ &= 1 + \frac{\omega_0^2}{16\bar{E}_n} \delta t^2. \end{aligned} \quad (\text{A7})$$